

Discontinuity-aware Normal Integration for Generic Central Camera Models

Francesco Milano^{1*} Manuel López-Antequera² Naina Dhingra² Roland Siegwart¹ Robert Thiel²
¹ETH Zurich, ²Meta

Abstract

Recovering a 3D surface from its surface normal map, a problem known as normal integration, is a key component for photometric shape reconstruction techniques such as shape-from-shading and photometric stereo. The vast majority of existing approaches for normal integration handle only implicitly the presence of depth discontinuities and are limited to orthographic or ideal pinhole cameras. In this paper, we propose a novel formulation that allows modeling discontinuities explicitly and handling generic central cameras. Our key idea is based on a local planarity assumption, that we model through constraints between surface normals and ray directions. Compared to existing methods, our approach more accurately approximates the relation between depth and surface normals, achieves state-of-the-art results on the standard normal integration benchmark, and is the first to directly handle generic central camera models.

1. Introduction

The problem of reconstructing a 3D surface from its surface normal map, also known as *normal integration*, has long been studied in computer vision. Its importance lies in its several applications for shape reconstruction, in particular as a necessary step to recover the surface from the output of photometric stereo [31] or shape-from-shading [18] techniques, which estimate normals from image shading.

Classically, normal integration has been studied predominantly under the assumption that the surface to be reconstructed is smooth [25]. This assumption, however, breaks in the presence of depth discontinuities, which naturally arise due to occlusions. While a number of methods for discontinuity-preserving integration have been proposed, these tend to introduce simplifying assumptions on the statistics of the discontinuities [3, 26] or model their magnitude only implicitly [1, 6, 32]. Moreover, the vast majority of the existing methods for discontinuity-preserving normal integration tackle the case of orthographic projection [3, 26, 33]; an exception is represented by the recently

proposed methods of BiNI [6] and of Kim *et al.* [22], which allow handling normals observed by an ideal pinhole camera, which more closely resembles real-world scenarios.

All the leading methods are derived from partial differential equations (PDEs) which relate normals to the depth map describing the surface, and typically base their formulation on functionals that discretely approximate these PDEs [6, 19, 22, 25]. In this work, we propose a novel formulation not derived from differential constraints, but based instead on the simple assumption that the surface is composed of local planes separated by discontinuities. We model this assumption through conditions between the surface normal and the *ray direction* associated with each pixel. We show experimentally that this results in a more accurate approximation of the ground-truth relation between depth and normals. Additionally, by relying on ray directions, our approach is to the best of our knowledge the first to directly handle generic central camera models, thereby extending the case of an ideal pinhole. Furthermore, our mathematical formulation explicitly takes discontinuities into account.

In order to recover both the depth map and the discontinuity values, we adopt an iterative optimization process based on the bilateral weighting scheme of BiNI. In particular, we adapt their semi-smooth assumption to our formulation and extend its optimization scheme to iteratively estimate depth and discontinuities. We additionally provide important novel insights on the optimization convergence, in light of our formulation. Experimental results show that our method captures discontinuities more accurately than existing methods and sets a new state of the art in the standard normal integration benchmark [28]. We provide extensive ablations on the hyperparameters of our method and further demonstrate it on normal maps from non-ideal pinhole cameras and real-world data, showing effective surface reconstruction also under these conditions.

In summary, our main contribution is a novel formulation for discontinuity-aware normal integration based on a local planarity assumption and ray directions, that: (i) more accurately describes the relation between depth and surface normals, (ii) achieves state-of-the-art results on the standard normal integration benchmark, and (iii) shows for the first time direct applicability to generic central camera models.

*Work mainly performed during an internship at Meta.

2. Related work

In the following Section, we briefly review the main existing approaches for normal integration. For a more extensive summary, we refer the reader to the surveys [25, 26].

The majority of normal integration methods proposed in the literature are derived from discrete approximations to PDEs relating depth and surface normals. One category of approaches, pioneered by Horn and Brooks [19], are based on constraints between the partial derivatives of the depth and the gradient field computed from the normal map [2, 3, 10, 14, 26]. More recently, an alternative differential formulation has been proposed by Zhu and Smith [34] and later extended by Cao *et al.* [6] that instead enforces an orthogonality constraint between the normals and the tangent plane to the surface, showing improved numerical stability. Our method is derived from a similar orthogonality constraint, but proposes a more general formulation that is applicable to generic central camera models and explicitly takes discontinuities into account.

To handle depth discontinuities, two main categories of approaches have been proposed that extend the PDE-based formulations above. One category of methods modify their functionals with robust estimators that reduce the effect of large residuals [3, 10, 24]. Another line of approaches instead introduce weights in the terms of the PDEs. Among these, single-analysis methods use weights defined before the optimization based on error residuals or input gradients [1, 12, 21, 30, 33]. Since the weights are kept fixed, these approaches might fail to correct wrong discontinuities during the optimization. To address this issue, alternative approaches have been proposed that iteratively optimize the weights. Typically, this is achieved by alternatively updating depth and parameters controlling the location of the discontinuities [2, 26, 32]. Recently, Cao *et al.* [6] significantly advanced the state of the art by proposing an iterative weight-update approach based on the assumption that the target surface is one-sided differentiable. At each iteration, the terms in its functional are scaled by relatively weighting the residuals on the two sides of each point, resulting in effective discontinuity preservation for the first time also for the perspective, ideal pinhole case. Kim *et al.* [22] later proposed to explicitly model gradients across discontinuities through auxiliary edges, showing more accurate detection of small discontinuities. In our approach, we adopt the bilateral weighting scheme of [6] and extend it to our formulation, which explicitly models discontinuities and handles generic central cameras.

3. Discontinuity-aware normal integration

Formally, the objective of normal integration is to recover a surface, in the form of a depth map, from a single-view per-pixel normal map and known camera parameters. Our

method tackles this problem by explicitly modeling surface discontinuities while solving for the unknown depth values. Additionally, unlike previous methods that are designed for orthographic and pinhole cameras, our approach allows modeling the broader category of central cameras.

In the following Section, we first derive the general formulation of our method for discontinuity-aware surface normal integration for arbitrary central cameras (Sec. 3.1). We then describe the general optimization framework to estimate solutions from our proposed formulation (Sec. 3.2). Finally, in Section 3.3 we provide specific details on how we perform the optimization and retrieve discontinuities by extending and generalizing the bilateral assumption of [6].

3.1. Proposed formulation

Let us consider a generic central camera, that is, any camera that models a *central projection* [15], and let us denote with $\tau : \mathbf{u} \in \mathbb{R}^2 \mapsto \boldsymbol{\tau}(\mathbf{u}) = (\tau_x(\mathbf{u}), \tau_y(\mathbf{u}), 1)^\top \in \mathbb{R}^3$ the mapping from a point $\mathbf{u} = (u, v)^\top$ on its image plane to its corresponding *ray direction vector* $\boldsymbol{\tau}(\mathbf{u})$. The elements $\tau_x(\mathbf{u})$ and $\tau_y(\mathbf{u})$ represent the tangent of the viewing angle, corresponding to the ray passing through \mathbf{u} , respectively along the x and y axes of the camera coordinate frame. For a generic point $\mathbf{p}(\mathbf{u})$ along the ray, with camera coordinates $(x(\mathbf{u}), y(\mathbf{u}), z(\mathbf{u}))^\top \in \mathbb{R}^3$, these can be expressed as $\tau_x(\mathbf{u}) = \frac{x(\mathbf{u})}{z(\mathbf{u})}$ and $\tau_y(\mathbf{u}) = \frac{y(\mathbf{u})}{z(\mathbf{u})}$. In the specific case of a pinhole camera with focal lengths f_x and f_y and principal point (c_x, c_y) , the mapping $\boldsymbol{\tau}$ is affine in the image coordinates and can be written as $\boldsymbol{\tau}(\mathbf{u}) = \left(\frac{u-c_x}{f_x}, \frac{v-c_y}{f_y}, 1 \right)^\top$.

When the camera observes a fully-opaque surface, each ray that intersects the surface is in one-to-one correspondence both with the visible 3D point $\mathbf{p} = (x, y, z)^\top \in \mathbb{R}^3$ at which it intersects the surface and with the normal vector $\mathbf{n}(\mathbf{p}) = (n_x, n_y, n_z)^\top \in \mathcal{S}^2 \subset \mathbb{R}^3$ at that point. It follows that it is possible to define injective mappings from image coordinates to visible surface points and normal vectors.

Our general formulation for normal integration, makes use of: (i) a local planarity approximation to handle pixel discretization, (ii) explicit discontinuity modelling, and (iii) the general definition of ray direction vectors. In particular, let a and b be two neighboring pixels in the input normal map, with corresponding image coordinates $\mathbf{u}_a = (u_a, v_a)^\top$ and $\mathbf{u}_b = (u_b, v_b)^\top$. In our main experiments, we define neighborhood based on 4-connectivity, although other connectivities can also be considered. Furthermore, let m denote a subpixel location along the line segment connecting pixel a and b on the image plane (Fig. 1) and let $\boldsymbol{\tau}_i = (\tau_{x_i}, \tau_{y_i}, 1)^\top$, $\mathbf{p}_i = (x_i, y_i, z_i)^\top$, and $\mathbf{n}_i = (n_{ix}, n_{iy}, n_{iz})^\top$ denote respectively the ray direction vector, the unknown visible surface point, and the known normal vector corresponding to (sub)pixel $i \in \{a, b, m\}$. Our method assumes that at the location of both a and b the sur-

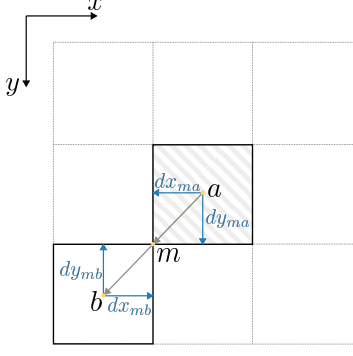


Figure 1. **Visualization of our local planarity assumption on the image plane.** For each pair of neighboring pixels a and b , a subpixel m is selected on the line segment connecting a and b , here chosen to be equidistant from the pixel centers. Along both the directions $m \rightarrow b$ and $m \rightarrow a$, the surface is assumed to be locally planar, with a discontinuity at the location of m .

face can be locally approximated by a plane segment perpendicular to the normal vector. More precisely, as illustrated in Fig. 2, we assume that the point p_m can be found at the intersection between the ray τ_m and the plane tangent to the surface at p_b . To model a depth discontinuity at p_m , we further assume that the plane tangent to the surface at point p_a can be intersected by moving from p_m by $\varepsilon_{b \rightarrow a}$ units along the positive direction of the z camera axis.

The assumptions described above can be modeled through the following system of 6 independent equations, where we define $dx_{ij} := x_i - x_j$, $dy_{ij} := y_i - y_j$, $dz_{ij} := z_i - z_j$, with $i, j \in \{a, b, m\}$, and use a right-hand convention for camera coordinates (x , y , and z axes pointing respectively to the right, bottom, and front):

$$\begin{cases} \tau_{x_m} = \frac{x_b + dx_{mb}}{z_b + dz_{mb}} \\ \tau_{y_m} = \frac{y_b + dy_{mb}}{z_b + dz_{mb}} \\ \tau_{x_a} = \frac{x_b + dx_{mb} - dx_{ma}}{z_b + dz_{mb} - dz_{ma}} \\ \tau_{y_a} = \frac{y_b + dy_{mb} - dy_{ma}}{z_b + dz_{mb} - dz_{ma}} \\ n_{bx} \cdot dx_{mb} + n_{by} \cdot dy_{mb} + n_{bz} \cdot dz_{mb} = 0 \\ n_{ax} \cdot dx_{ma} + n_{ay} \cdot dy_{ma} + n_{az} \cdot (dz_{ma} + \varepsilon_{b \rightarrow a}) = 0 \end{cases} \quad (1)$$

The first four equations in the system follow by the definition of ray direction vector, while the last two model the perpendicularity constraint between the two plane segments and the normal vectors \mathbf{n}_a , \mathbf{n}_b , taking into account the depth discontinuity $\varepsilon_{b \rightarrow a}$.

Solving (1) for dx_{ma} , dx_{mb} , dy_{ma} , dy_{mb} , dz_{ma} , dz_{mb} , and plugging the solutions back into the definitions of these quantities yields the following condition on z_a , z_b , and $\varepsilon_{b \rightarrow a}$:

$$z_a = \omega_{\varepsilon_a} \cdot \varepsilon_{b \rightarrow a} + \omega_{b \rightarrow a} \cdot z_b, \quad (2)$$

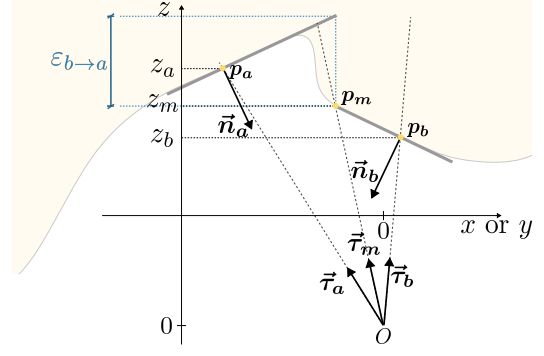


Figure 2. **Visualization of our local planarity assumption in 3D.** We assume that the surface can be modeled as piecewise-planar and define the plane endpoints as the intersection between the surface and the rays from the camera center of projection O along the ray directions τ_a , τ_b , and τ_m . We explicitly model a discontinuity $\varepsilon_{b \rightarrow a}$ along the z camera axis in line with p_m .

where

$$\begin{aligned} \omega_{\varepsilon_a} &= \frac{n_{az}}{\mathbf{n}_a^\top \boldsymbol{\tau}_a} \\ \omega_{b \rightarrow a} &= \frac{\mathbf{n}_a^\top \boldsymbol{\tau}_m \cdot \mathbf{n}_b^\top \boldsymbol{\tau}_b}{\mathbf{n}_a^\top \boldsymbol{\tau}_a \cdot \mathbf{n}_b^\top \boldsymbol{\tau}_m}. \end{aligned} \quad (3)$$

We provide a full derivation of (3) in Appendix A.

It should be noted that all the quantities in (3) are known by hypothesis, except for τ_m (or equivalently the location of the subpixel m on the image plane), the choice of which controls the local planarity approximation (Fig. 2). In our main experiments, we assume for simplicity that $\tau_m = (\tau_a + \tau_b)/2$, which for mappings τ that are affine in the image coordinates corresponds to m having image coordinates given by the average of the pixel coordinates of a and b , i.e., $\mathbf{u}_m = (\mathbf{u}_a + \mathbf{u}_b)/2$. However, alternative choices for obtaining τ_m are possible, including through linear interpolation $\tau_m = \tau_a + \lambda_m(\tau_b - \tau_a)$, with $\lambda_m \in [0, 1]$ (of which the above is a special case, with $\lambda_m = 0.5$ for all pixel pairs). We refer the reader to Appendix D in the Supplementary Material for a more detailed analysis and for ablations on the choice of τ_m .

We furthermore note that the coefficients in (3) depend on terms of the form $\mathbf{n}^\top \boldsymbol{\tau}$, which relate surface normals to ray directions through a dot product. This dot product relationship has previously been studied in the literature, famously by Marr [23] and more recently by Bae and Davison [4]. As previously noted in these works, a necessary condition for a surface point to be visible is that the angle between its corresponding ray direction vector and surface normal vector is greater than 90° , i.e., $\mathbf{n}^\top \boldsymbol{\tau} < 0$, with equality being attained in the limit of the point lying on an occluding boundary. It follows that, assuming valid surface normals, the terms $\mathbf{n}_a^\top \boldsymbol{\tau}_a$ and $\mathbf{n}_b^\top \boldsymbol{\tau}_b$ in (3) are strictly negative. On the other hand, the terms $\mathbf{n}_a^\top \boldsymbol{\tau}_m$ and $\mathbf{n}_b^\top \boldsymbol{\tau}_m$ are

negative if the points of intersection between the ray direction τ_m and the two local planes containing p_a and p_b , respectively, are visible by the camera when approximating the surface as local planes. As we discuss more in detail in Appendix C, when choosing τ_m to linearly interpolate τ_a and τ_b the latter condition is fulfilled for all but very specific corner cases, and is always verified in practice for $\tau_m = (\tau_a + \tau_b)/2$. From (3), it follows that under these settings the $\omega_{b \rightarrow a}$ terms are always positive. While this condition is not strictly necessary, it allows a convenient reformulation of (2), as detailed in the next Section.

3.2. General solution framework

Similarly to previous methods [6, 22], our formulation allows estimating the unknown depth values by solving a least-squares optimization problem. In particular, the set of conditions (2) for all valid choices of neighboring pixels (a, b) , (a, c) , *etc.* can be rewritten in the form of a system of linear equations $\mathbf{A}\mathbf{z} = \mathbf{b}$, where

$$\mathbf{A} = \begin{bmatrix} 1 & -\omega_{b \rightarrow a} & 0 & \cdots \\ 1 & 0 & -\omega_{c \rightarrow a} & \cdots \\ \vdots & \vdots & \vdots & \ddots \\ -\omega_{a \rightarrow b} & 1 & 0 & \cdots \\ \vdots & \vdots & \vdots & \ddots \end{bmatrix}, \quad (4)$$

$$\mathbf{z} = \begin{bmatrix} z_a \\ z_b \\ z_c \\ \vdots \end{bmatrix}, \text{ and } \mathbf{b} = \begin{bmatrix} \omega_{\varepsilon_a} \cdot \varepsilon_{b \rightarrow a} \\ \omega_{\varepsilon_a} \cdot \varepsilon_{c \rightarrow a} \\ \vdots \\ \omega_{\varepsilon_b} \cdot \varepsilon_{a \rightarrow b} \\ \vdots \end{bmatrix}.$$

The optimization problem then reads as:

$$\min_{\mathbf{z}} (\mathbf{A}\mathbf{z} - \mathbf{b})^\top \mathbf{W} (\mathbf{A}\mathbf{z} - \mathbf{b}), \quad (5)$$

where \mathbf{W} is an optional diagonal matrix that can assign different weights to the equations. The unknown depth values \mathbf{z} can then be found by applying an iterative conjugate gradient method [6, 16] on the normal equation of (5), $\mathbf{A}^\top \mathbf{W} \mathbf{A} \mathbf{z} = \mathbf{A}^\top \mathbf{W} \mathbf{b}$. However, since our formulation explicitly takes discontinuities into account, the term \mathbf{b} in (5) depends on the values $\varepsilon_{b \rightarrow a}$, $\varepsilon_{c \rightarrow a}$, *etc.* We note that if the ground-truth values of these quantities – hence of the term \mathbf{b} – were known, the conditions expressed by the system $\mathbf{A}\mathbf{z} = \mathbf{b}$ would model *exactly* the relationship between the ground-truth depth values at the different pixels, and as we show in Section 4.3, the optimization would be able to recover the ground-truth depth values with close-to-perfect accuracy. Since, however, the ground-truth values for $\varepsilon_{b \rightarrow a}$ are unknown, in our optimization we not only iteratively update the depth values, but also optimize the term \mathbf{b} , so that it progressively models the ground-truth term more closely.

More in detail, upon initialization we assume the surface to be smooth everywhere, thereby setting all discontinuities $\varepsilon_{b \rightarrow a}$ to 0. As a consequence, the system of equations (4) is initially homogeneous; knowing that depth values are positive and following a common practice in the literature [6, 25], we therefore introduce the change of variable $\tilde{z} := \log z$. To allow rewriting (2) as a condition on \tilde{z}_a and \tilde{z}_b , we additionally express the discontinuity values as *relative* discontinuities, by introducing the terms $\alpha_{b \rightarrow a} := \varepsilon_{b \rightarrow a}/z_b$, so that

$$\varepsilon_{b \rightarrow a} = \alpha_{b \rightarrow a} \cdot z_b. \quad (6)$$

Using (6) and applying the logarithm to both sides of (2), we can rewrite our condition (2) as

$$\tilde{z}_a^{(t)} = \log \left(\omega_{\varepsilon_a} \cdot \alpha_{b \rightarrow a}^{(t)} + \omega_{b \rightarrow a} \right) + \tilde{z}_b^{(t)}, \quad (7)$$

where we additionally use the superscript (t) to indicate that the variables are evaluated at iteration t of the optimization.

We note that upon initialization the terms inside the logarithm in (7) coincide with $\omega_{b \rightarrow a}$, having set $\varepsilon_{b \rightarrow a}^{(0)} = 0$ and therefore $\alpha_{b \rightarrow a}^{(0)} = 0$. As noted in Section 3, when choosing the subpixel locations m to interpolate between a and b , the terms $\omega_{b \rightarrow a}$ are positive, which ensures that the logarithm is always defined. Similarly to [6, 22], we initialize the log-depth values $\tilde{z}_a^{(t)}$, $\tilde{z}_b^{(t)}$, *etc.* to 0, which corresponds to a planar surface of unit depth. At each iteration t , we first optimize the log-depth values using the system of equations $\tilde{\mathbf{A}}\tilde{\mathbf{z}} = \tilde{\mathbf{b}}$ that can be derived from (7) with the same procedure used to write (4) from (2); then, we update the terms $\alpha_{b \rightarrow a}^{(t)}$, as we detail in the next Section.

3.3. Discontinuity-aware bilateral formulation

In order to guide the optimization of the log-depth values as well as to iteratively update the discontinuity values, we adopt the semi-smooth assumption of BiNI [6], which we extend to our formulation and briefly summarize below.

For a pinhole camera with focal lengths f_x and f_y and principal point (c_x, c_y) , BiNI makes use of the following discrete PDE, here expressed in our notation:

$$\gamma_{b \rightarrow a}(\tilde{z}_a - \tilde{z}_b) = \delta_{b \rightarrow a}, \quad (8)$$

where neighboring pixels b are defined according to 4-connectivity, and the terms $\gamma_{b \rightarrow a}$ and $\delta_{b \rightarrow a}$ are defined as:

$$\gamma_{b \rightarrow a} = n_{ax}(u_a - c_x) + n_{ay}(v_a - c_y) + n_{az}f, \quad (9)$$

with $f = f_x$, $\delta_{b \rightarrow a} = \pm n_{ax}$ for neighboring pixels b s.t. $(u_b, v_b) = (u_a \pm 1, v_a)$ and $f = f_y$, $\delta_{b \rightarrow a} = \pm n_{ay}$ for neighboring pixels b s.t. $(u_b, v_b) = (u_a, v_a \pm 1)$. Their method then assumes the surface to be semi-smooth, that is,

to contain at most one-sided discontinuities. This assumption is modeled by weighting each equation (8), at each optimization iteration t , by a term

$$w_{b \rightarrow a}^{\text{BiNI}(t)} = \sigma_k \left(\left(\text{res}_{-b \rightarrow a}^{(t)} \right)^2 - \left(\text{res}_{b \rightarrow a}^{(t)} \right)^2 \right), \quad (10)$$

where $\text{res}_{b \rightarrow a}^{(t)} := \gamma_{b \rightarrow a} \left(\tilde{z}_a^{(t)} - \tilde{z}_b^{(t)} \right)$ is a residual that encodes the extent to which the surface is discontinuous between \mathbf{p}_b and \mathbf{p}_a , $\sigma_k(\cdot)$ is the sigmoid function $\sigma_k(x) = (1 + e^{-kx})^{-1}$, and where we denote with $-b$ the neighbor of a opposite to b , i.e. s.t. $\mathbf{u}_{-b} - \mathbf{u}_a = -(\mathbf{u}_b - \mathbf{u}_a)$. By properties of the sigmoid function, $w_{b \rightarrow a}^{\text{BiNI}(t)} \in [0, 1]$ and $w_{-b \rightarrow a}^{\text{BiNI}(t)} = 1 - w_{b \rightarrow a}^{\text{BiNI}(t)}$, with $w_{b \rightarrow a}^{\text{BiNI}(t)} \approx 0$ indicating that the estimated surface is discontinuous between \mathbf{p}_b and \mathbf{p}_a but continuous between \mathbf{p}_{-b} and \mathbf{p}_a , and $w_{b \rightarrow a}^{\text{BiNI}(t)} \approx w_{-b \rightarrow a}^{\text{BiNI}(t)} \approx 0.5$ that the surface is continuous on both sides.

We note that, up to the multiplicative constant $\gamma_{b \rightarrow a}$, the formulation of BiNI (8) has the same functional form as our formulation. While (8) could be rewritten as $\tilde{z}_a - \tilde{z}_b = \delta_{b \rightarrow a} / \gamma_{b \rightarrow a}$, as noted in Sec. 2 of the Supplementary of BiNI [8] the factor $\gamma_{b \rightarrow a}$ proves to be crucial to improving their numerical stability during optimization. We empirically verify that the same holds true for our formulation, and we therefore rewrite our formulation as follows, by multiplying both sides of (7) by $\gamma_{b \rightarrow a}$ and rearranging:

$$\gamma_{b \rightarrow a} (\tilde{z}_a - \tilde{z}_b) = \gamma_{b \rightarrow a} \log (\omega_{b \rightarrow a} + \omega_{\varepsilon_a} \cdot \alpha_{b \rightarrow a}). \quad (11)$$

Following BiNI, we furthermore define our weighting matrix \mathbf{W} based on (10). Importantly, we additionally note that $\gamma_{b \rightarrow a}$ can be rewritten (up to the differences between f_x and f_y) as

$$\gamma_{b \rightarrow a} = f \cdot \mathbf{n}_a^\top \boldsymbol{\tau}_a, \quad (12)$$

which for generic central cameras we generalize as

$$\gamma_{b \rightarrow a} = \|\mathbf{u}_b - \mathbf{u}_a\| / \|\boldsymbol{\tau}_b - \boldsymbol{\tau}_a\| \cdot \mathbf{n}_a^\top \boldsymbol{\tau}_a. \quad (13)$$

In light of this observation, we present a thorough analysis of the impact of the terms in (13) in Appendix B, providing important novel findings about their effect on convergence and shedding light on the role of $\gamma_{b \rightarrow a}$ in the optimization.

While the above procedure allows optimizing the log-depth values, as noted in Sec. 3.2 we would like to additionally update our discontinuity terms $\alpha_{b \rightarrow a}^{(t)}$, to model discontinuities with increasingly higher accuracy. To this purpose, we invert (7) to derive the following update scheme:

$$\alpha_{b \rightarrow a}^{(t+1)} \leftarrow \left(\exp \left(\tilde{z}_a^{(t)} - \tilde{z}_b^{(t)} \right) - \omega_{b \rightarrow a} \right) / \omega_{\varepsilon_a}, \quad (14)$$

with $\alpha_{b \rightarrow a}^{(0)} = 0$ for all valid pairs (a, b) . However, applying this update to all pairs would cause the optimization to converge in one iteration to a suboptimal solution, since its objective (5) would evaluate to 0. To avoid this, we introduce

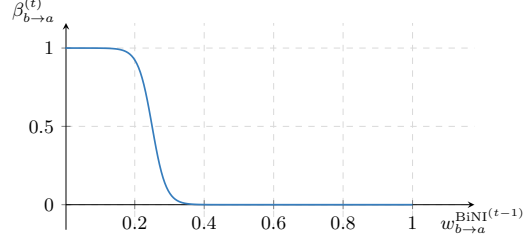


Figure 3. **Discontinuity activation term (16) for $q = 50.0$ and $\rho = 0.25$.** The term $\beta_{b \rightarrow a}^{(t)}$ progressively incorporates discontinuities in our formulation, which correspond to $w_{b \rightarrow a}^{\text{BiNI}(t-1)} < 0.5$.

an additional term $\beta_{b \rightarrow a}^{(t)} \in [0, 1]$ in (11), which selectively activates the discontinuity terms, as follows:

$$\gamma_{b \rightarrow a} \left(\tilde{z}_a^{(t)} - \tilde{z}_b^{(t)} \right) = \gamma_{b \rightarrow a} \log \left(\omega_{b \rightarrow a} + \omega_{\varepsilon_a} \cdot \alpha_{b \rightarrow a}^{(t)} \cdot \beta_{b \rightarrow a}^{(t)} \right). \quad (15)$$

The rationale for $\beta_{b \rightarrow a}^{(t)}$ is the following: If the surface is estimated to be continuous between pixels a and b , one can approximate $\alpha_{b \rightarrow a} \approx 0$, so the influence of the discontinuity term should be negligible. On the other hand, the more the surface is estimated to be discontinuous between a and b , the more the term $\alpha_{b \rightarrow a}$ would increase the accuracy of (11), and thus the more it should be taken into account. We note that the weights $w_{b \rightarrow a}^{\text{BiNI}}$ naturally model this relationship. Indeed, as the optimization identifies with increasing confidence that a discontinuity is present between a and b the corresponding term $w_{b \rightarrow a}^{\text{BiNI}}$ increasingly approaches 0. Viceversa, if the optimization identifies the surface to be continuous between a and b , or at least equally discontinuous in the directions of the two opposite pixels b and $-b$, the term $w_{b \rightarrow a}^{\text{BiNI}}$ is greater or equal than 0.5 ($w_{b \rightarrow a}^{\text{BiNI}} \rightarrow 1$ in the first case and $w_{b \rightarrow a}^{\text{BiNI}} \approx 0.5$ in the latter). We therefore define the *discontinuity activation* terms as

$$\beta_{b \rightarrow a}^{(t)} = \sigma \left(q \cdot \left(\rho - w_{b \rightarrow a}^{\text{BiNI}(t-1)} \right) \right), \quad (16)$$

where we set $q = 50.0$ and $\rho = 0.25$, which guarantees that $\beta_{b \rightarrow a}^{(t)}$ tends smoothly to 1 as $w_{b \rightarrow a}^{\text{BiNI}(t-1)} \rightarrow 0$ and smoothly to 0 as $w_{b \rightarrow a}^{\text{BiNI}(t-1)} \rightarrow 0.5^-$ (cf. Fig. 3). We study the impact of the hyperparameters q and ρ in Appendix E.

4. Experiments

This Section provides the experimental evaluation of our method, describing our experimental setup (Sec. 4.1), comparing the accuracy of its formulation to that of existing ones (Sec. 4.2), evaluating its normal integration accuracy on a standard benchmark (Sec. 4.3), and demonstrating its applicability to generic central cameras (Sec. 4.4) and real-world input normals (Sec. 4.5). Readers can find ablations, additional experimental results, and a discussion of the limitations of our method in the Supplementary Material.

4.1. Experimental settings

Baselines. We compare our method to the state-of-the-art BiNI [6] and Kim *et al.* [22] on the DiLiGenT benchmark [28]. As no source code is publicly available for [22], in the remaining evaluations we only compare our method to BiNI, setting its hyperparameter to its default value.

Hardware and timing. We run all our evaluations on a standard CPU-only machine, on which our unoptimized implementation takes between 50 and 120 seconds for 1200 iterations with an input normal map of size 512×612 .

4.2. Comparison of formulation accuracy

Before examining the quality of the reconstruction produced by our optimization, we assess how accurately our formulation approximates the ground-truth relation between depth and surface normals compared to existing PDE-derived formulations. To this end, we compute for both our method and BiNI the absolute residual emerging from the respective formulations; as previously noted, this has for both the same functional form $|\gamma_{b \rightarrow a}(\tilde{z}_a - \tilde{z}_b) - \text{RHS}|$, where RHS denotes the right-hand side of (8) for BiNI and of (11) for our method. We evaluate this quantity on the DiLiGenT dataset [28], assuming for fairness unknown discontinuity values, thereby setting the terms $\alpha_{b \rightarrow a}$ in our formulation to 0. As shown in Tab. 1, our method achieves mean error lower by one or two orders of magnitude on all but one object. We provide additional comparisons using relative residuals in Appendix G, where we find similar results.

4.3. Benchmark experiments

We evaluate the reconstruction accuracy of our normal integration method compared to the state-of-the-art approaches [6] and [22] on the standard DiLiGenT benchmark [28], which provides ground-truth normal maps produced by an ideal pinhole camera. As shown by Fig. 5 and Tab. 2, our method without discontinuity computation (*i.e.*, setting $\alpha_{b \rightarrow a} = 0$) achieves accuracy that is state-of-the-art for 7 out of 9 objects, comparable for 1 object, and worse for a single object. This result shows that the higher accuracy of our formulation can effectively translate into better reconstruction quality through the optimization process. This is further confirmed by verifying that using coefficients based on discontinuity values $\alpha_{b \rightarrow a}$ from the ground-truth surface, the optimization results in an extremely low error for virtually all the objects. We note that our method converges more slowly than BiNI, and we therefore run it for a larger number of iterations (1200); however, after the same number of iterations necessary for BiNI to achieve convergence (150) our method already achieves better results than the other approaches on most objects. Iterative computation of the terms $\alpha_{b \rightarrow a}$ allows more accurately capturing discontinuities (Fig. 6) and further reduces the reconstruc-

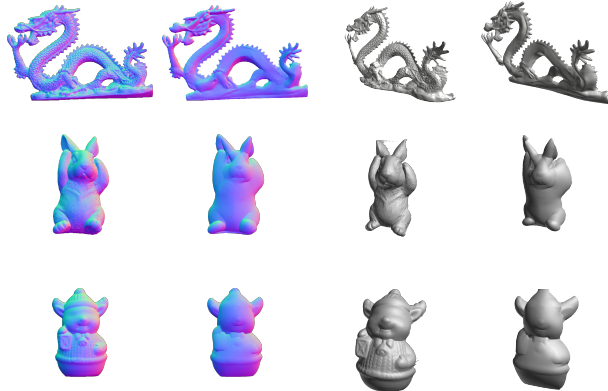


Figure 4. **Reconstructions of our method from real-world data.** From the left, the third and fourth column show our reconstruction based on normals respectively from photometric stereo [20] (first column) and from DSINE [4] (second column).

tion error, resulting in state of the art on virtually all objects. Further, object-specific improvements can be obtained by tuning the hyperparameters of our discontinuity activation term (*cf.* Appendix E).

4.4. Experiments with non-ideal pinhole cameras

To verify the applicability of our method to generic central camera models, we synthetically render normal maps (and depth for evaluation) observed by a pinhole camera with Brown-Conrady lens distortion [5], using BlenderProc [9]. Since to our knowledge no other methods are available that can directly handle normals from non-ideal pinhole cameras, we show, for illustration purposes only, the output of BiNI for such distorted maps; we remark that a quantitative evaluation is unfair, since BiNI assumes normals from an ideal pinhole camera. We additionally render the normal and depth maps observed by an ideal pinhole camera with intrinsics resulting from undistortion and resolution matching the original one. As shown in Fig. 7, our method effectively handles the case with lens distortion both for scene-level maps of medium complexity and for object-level ones, while the reconstruction from BiNI suffers from noticeable distortion, as expected. The undistorted reconstructions show comparable results between the two methods, with slightly better accuracy for ours, but at the cost of a reduced field of view, due to barrel distortion.

4.5. Experiments with real-world data

Figure 4 shows qualitative examples of the reconstructions produced by our method using normals obtained from real-world images [20], both through a recent photometric stereo approach [20] and through prediction by a state-of-the-art learning-based normal estimation method [4]. The results indicate that our method can be applied effectively to real-world normal maps, producing reasonably accurate reconstructions also for the overly smooth normals of [4].

Method	bear	buddha	cat	cow	harvest	pot1	pot2	reading	goblet
BiNI [6]	$(3.72 \pm 2.71) \times 10^{-1}$	$(4.57 \pm 9.21) \times 10^{-1}$	$(0.54 \pm 1.09) \times 10^0$	$(4.46 \pm 3.58) \times 10^{-1}$	$(0.52 \pm 2.71) \times 10^0$	$(4.18 \pm 5.63) \times 10^{-1}$	$(3.96 \pm 4.26) \times 10^{-1}$	$(0.50 \pm 1.24) \times 10^0$	$(0.43 \pm 1.33) \times 10^0$
Ours	$(0.82 \pm 7.39) \times 10^{-2}$	$(0.90 \pm 9.12) \times 10^{-1}$	$(0.03 \pm 1.27) \times 10^0$	$(0.19 \pm 1.61) \times 10^{-1}$	$(0.22 \pm 2.80) \times 10^0$	$(0.09 \pm 2.72) \times 10^0$	$(0.39 \pm 3.11) \times 10^{-1}$	$(0.08 \pm 1.21) \times 10^0$	$(0.06 \pm 1.20) \times 10^0$

Table 1. **Absolute formulation accuracy on the ground-truth log-depth map, DiLiGenT dataset [28].** For both methods, we report mean and standard deviation across the pixels of the absolute residual $|\gamma_{b \rightarrow a}(\tilde{z}_a - \tilde{z}_b) - \text{RHS}|$ computed on the ground-truth log-depth map, where RHS denotes the right-hand side of (8) for BiNI and (11) for Ours. We use $\tau_m = (\tau_a + \tau_b)/2$ and $\alpha_{b \rightarrow a} = 0$ for Ours.

Method	bear	buddha	cat	cow	harvest	pot1	pot2	reading	goblet*
BiNI [6] – From paper	0.49	0.86	0.11	<u>0.07</u>	2.73	0.62	0.22	0.34	8.53
BiNI [6] – From code [7], 1200 iterations †	0.33	1.06	<u>0.07</u>	0.06	1.84	0.64	0.22	0.26	9.00
Kim <i>et al.</i> [22]	0.45	0.67	0.24	0.06	2.44	0.57	0.19	0.15	9.02
Ours w/o $\alpha_{b \rightarrow a}$ computation, 150 iterations	0.08	0.30	0.06	0.09	4.98	0.52	0.13	0.21	6.46
Ours w/o $\alpha_{b \rightarrow a}$ computation, 1200 iterations	<u>0.07</u>	<u>0.26</u>	0.06	0.08	4.83	<u>0.50</u>	0.13	0.12	6.56
Ours, 150 iterations	0.03	0.37	0.06	0.08	<u>1.35</u>	<u>0.50</u>	<u>0.14</u>	<u>0.15</u>	<u>5.98</u>
Ours, 1200 iterations	0.03	0.24	0.06	0.08	0.73	0.49	0.13	0.17	4.72
Ours with known discontinuity values	0.01	0.10	0.03	$< 10^{-2}$	0.34	0.04	0.03	0.08	0.11

Table 2. **Mean absolute depth error (MADE) [mm] on the DiLiGenT benchmark [28].** For each object, **bold** and underlined denote respectively the best and the second-best result across the methods. The results of Kim *et al.* are taken from [22]. *This object contains a full depth discontinuity. † BiNI achieves full convergence already after 150 iterations.

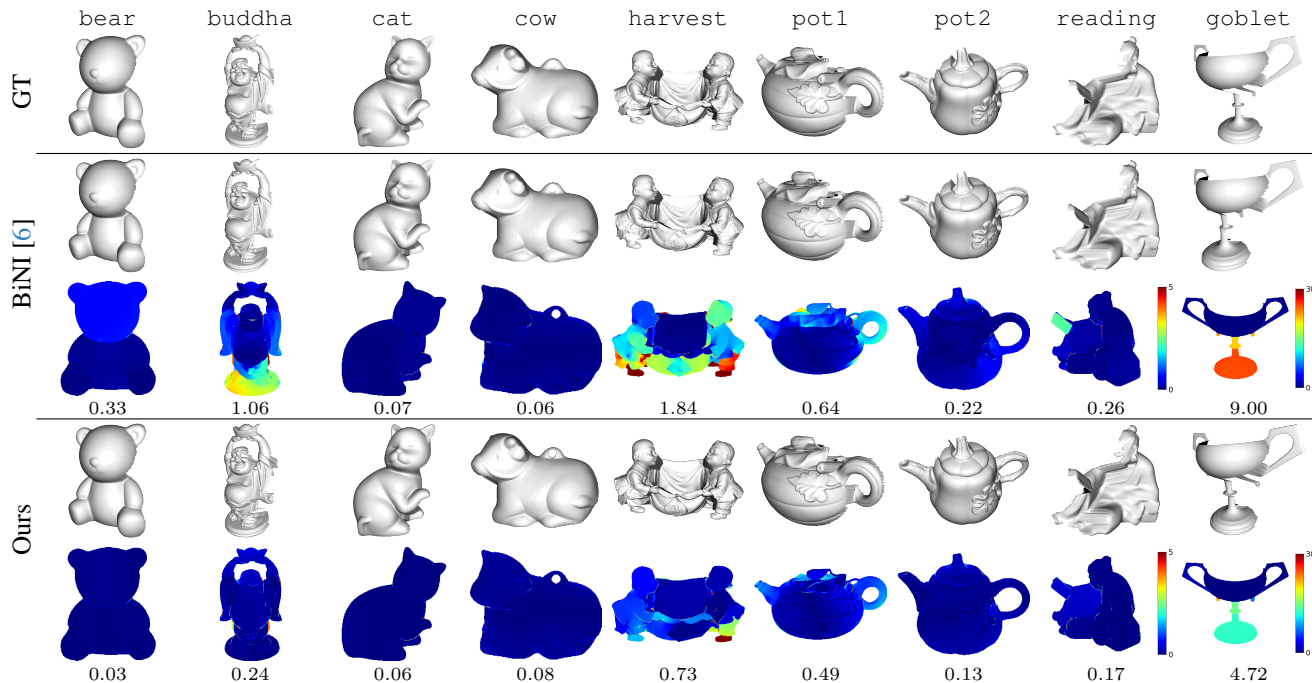


Figure 5. **Comparison on the DiLiGenT benchmark [28].** First row: Ground-truth surfaces. Second and third row: Surface reconstructed by BiNI [6]; absolute depth errors maps (in mm). Fourth and fifth row: Surface reconstructed by our method with explicit discontinuity computation; absolute depth error maps. The color map is the same for the first eight columns. Below each absolute depth error map is the corresponding mean value (MADE) in mm.

5. Conclusions

We presented a novel formulation for normal integration based on a local planarity assumption modeled through ray directions and explicit discontinuity terms. Compared to existing methods, our approach more accurately approxi-

mates the relation between depth and surface normals and achieves state-of-the-art results on the standard benchmark for normal integration. Furthermore, thanks to its formulation based on ray directions, our method allows for the first time handling normal maps from generic central camera models.

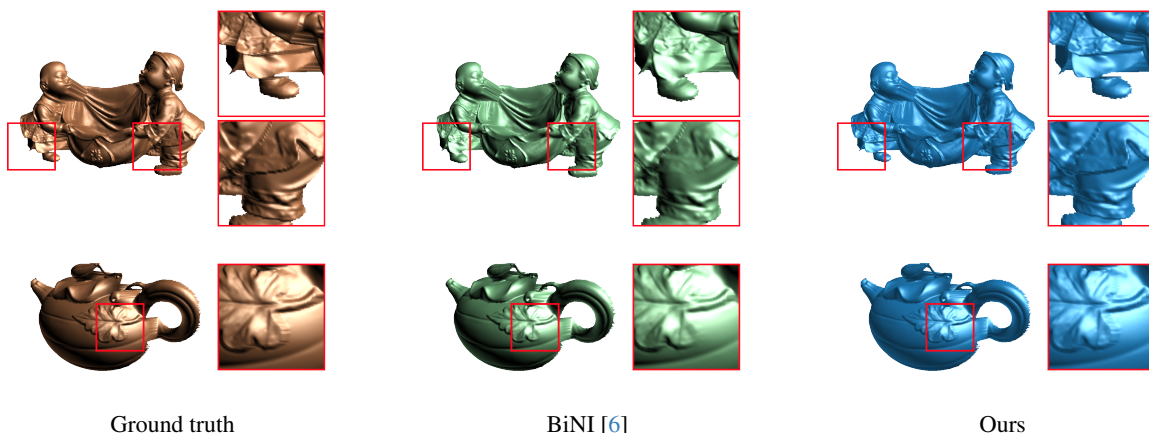


Figure 6. **Detail of the reconstructed surfaces.** Our formulation allows capturing discontinuities with higher accuracy than the previous method of BiNI [6]. Top and bottom rows show respectively objects *harvest* and *pot1* from the DiLiGenT benchmark [28].

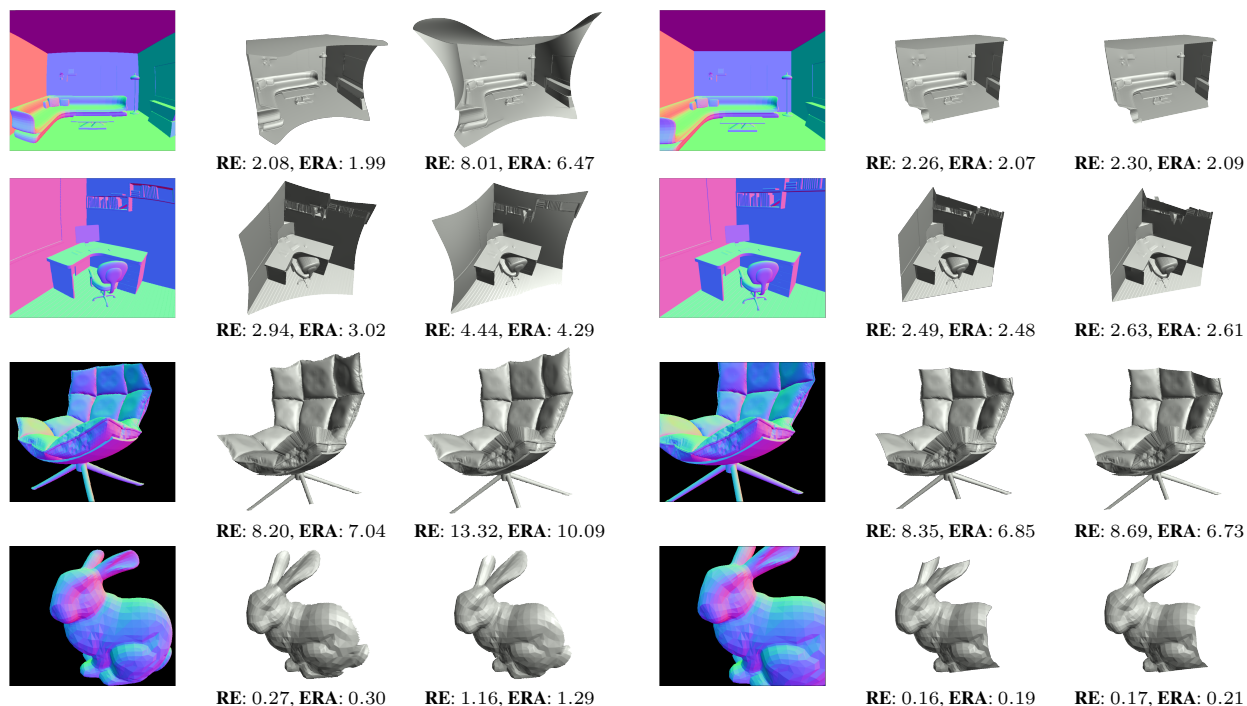


Figure 7. **Reconstructions for non-ideal pinhole normal maps.** From the left, first three columns: input normal map with Brown-Conrady distortion, reconstruction of our method, and reconstruction of BiNI; last three columns: undistorted input normal map, reconstruction of our method, reconstruction of BiNI. Below each reconstruction are the corresponding mean relative depth error (RE) and mean depth error relative to the average depth of the scene (ERA), both expressed as percentages. Note that undistortion causes part of the scene to be cropped. Source of the mesh models from the top to the bottom row: [11], [17], [13] [29].

References

- [1] Amit Agrawal, Rama Chellappa, and Ramesh Raskar. [An Algebraic Approach to Surface Reconstruction from Gradient Fields.](#) In *ICCV*, 2005. 1, 2
- [2] Amit Agrawal, Ramesh Raskar, and Rama Chellappa. [What](#)
- [3] Hicham Badri, Hussein Yahia, and Driss Aboutajdine. [Robust Surface Reconstruction via Triple Sparsity.](#) In *CVPR*, 2014. 1, 2

[Is the Range of Surface Reconstructions from a Gradient Field?](#) In *ECCV*, 2006. 2

- [4] Gwangbin Bae and Andrew J. Davison. [Rethinking Inductive Biases for Surface Normal Estimation](#). In *CVPR*, 2024. 3, 6, 18
- [5] Duane C. Brown. [Decentering Distortion of Lenses](#). *Photogrammetric Engineering*, 32(3):444–462, 1966. 6
- [6] Xu Cao, Hiroaki Santo, Boxin Shi, Fumio Okura, and Yasuyuki Matsushita. [Bilateral Normal Integration](#). In *ECCV*, 2022. 1, 2, 4, 6, 7, 8, 10, 14, 15, 18
- [7] Xu Cao, Hiroaki Santo, Boxin Shi, Fumio Okura, and Yasuyuki Matsushita. [Bilateral Normal Integration – Official implementation](#). https://github.com/xucaoc42/bilateral_normal_integration, 2022. Accessed: 2025-01-27. 7
- [8] Xu Cao, Hiroaki Santo, Boxin Shi, Fumio Okura, and Yasuyuki Matsushita. [Bilateral Normal Integration – Supplementary material](#). https://doi.org/10.1007/978-3-031-19769-7_32#Sec12, 2022. Accessed: 2025-02-07. 5, 10, 14, 18
- [9] Maximilian Denninger, Dominik Winkelbauer, Martin Sundermeyer, Wout Boerdijk, Markus Knauer, Klaus H. Strobl, Matthias Humt, and Rudolph Triebel. [BlenderProc2: A Procedural Pipeline for Photorealistic Rendering](#). *Journal of Open Source Software*, 8(82):4901, 2023. 6
- [10] Jean-Denis Durou, Jean-François Aujol, and Frédéric Courteille. [Integrating the Normal Field of a Surface in the Presence of Discontinuities](#). In *CVPRW*, 2009. 2
- [11] dylanheyes. Mesh “White Modern Living Room”. <https://sketchfab.com/3d-models/white-modern-living-room-afb8cb0cbee1488caf61471ef14041e9>, 2023. CC BY 4.0. 8
- [12] Roberto Fraile and Edwin R. Hancock. [Combinatorial Surface Integration](#). In *ICPR*, 2006. 2
- [13] Grapxly. Mesh “Office Chair”. <https://sketchfab.com/3d-models/office-chair-f8c9ea4a5dba410ca6e511199dd62b48>, 2023. CC BY 4.0. 8
- [14] Matthew Harker and Paul O’Leary. [Least Squares Surface Reconstruction from Measured Gradient Fields](#). In *CVPR*, 2008. 2
- [15] Richard Hartley and Andrew Zisserman. [Multiple View Geometry in Computer Vision](#), page 6. Cambridge University Press, 2nd edition, 2004. 2
- [16] Magnus R. Hestenes and Eduard Stiefel. [Methods of Conjugate Gradients for Solving Linear Systems](#). *Journal of Research of the National Bureau of Standards*, 49(6):409–436, 1952. 4
- [17] Vladyslav Holhanov. Mesh “Office”. <https://sketchfab.com/3d-models/office-28fd69fff714343f2bd278a2572774323>, 2021. CC BY 4.0. 8
- [18] Berthold K.P Horn. [Obtaining Shape from Shading Information](#). *The Psychology of Computer Vision*, pages 115–155, 1975. 1
- [19] Berthold K.P Horn and Michael J Brooks. [The Variational Approach to Shape from Shading](#). *Computer Vision, Graphics, and Image Processing*, 33(2):174–208, 1986. 1, 2
- [20] Satoshi Ikehata. [Scalable, Detailed and Mask-free Universal Photometric Stereo](#). In *CVPR*, 2023. 6
- [21] Bilge Karaçalı and Wesley Snyder. [Reconstructing discontinuous surfaces from a given gradient field using partial integrability](#). *Computer Vision and Image Understanding*, 92(1):78–111, 2003. 2
- [22] Hyomin Kim, Yucheol Jung, and Seungyong Lee. [Discontinuity-preserving Normal Integration with Auxiliary Edges](#). In *CVPR*, 2024. 1, 2, 4, 6, 7, 18
- [23] David Marr. [Analysis of occluding contour](#). *Proceedings of the Royal Society of London. Series B. Biological Sciences*, 197(1129):441–475, 1977. 3
- [24] Yvain Quéau and Jean-Denis Durou. [Edge-Preserving Integration of a Normal Field: Weighted Least-Squares, TV and \$L^1\$ Approaches](#). In *Int. Conf. Scale Space Variat. Methods in Comp. Vis.*, 2015. 2
- [25] Yvain Quéau, Jean-Denis Durou, and Jean-François Aujol. [Normal Integration: A Survey](#). *Journal of Mathematical Imaging and Vision*, 60:576–593, 2018. 1, 2, 4, 18
- [26] Yvain Quéau, Jean-Denis Durou, and Jean-François Aujol. [Variational Methods for Normal Integration](#). *Journal of Mathematical Imaging and Vision*, 60:609–632, 2018. 1, 2
- [27] Srikumar Ramalingam, Peter Sturm, and Suresh K. Lodha. [Theory and Calibration for Axial Cameras](#). In *ACCV*, 2006. 18
- [28] Boxin Shi, Zhe Wu, Zhipeng Mo, Dinglong Duan, Sai-Kit Yeung, and Ping Tan. [A Benchmark Dataset and Evaluation for Non-Lambertian and Uncalibrated Photometric Stereo](#). In *CVPR*, 2016. 1, 6, 7, 8, 12, 14, 15, 16, 17
- [29] Greg Turk and Marc Levoy. Mesh “Stanford Bunny”. <https://graphics.stanford.edu/data/3Dscanrep/>, 1994. 8
- [30] Yinting Wang, Jiajun Bu, Na Li, Mingli Song, and Ping Tan. [Detecting Discontinuities for Surface Reconstruction](#). In *ICPR*, 2012. 2
- [31] Robert J. Woodham. [Photometric Method For Determining Surface Orientation From Multiple Images](#). *Optical Engineering*, 19(1):139–144, 1980. 1
- [32] Tai-Pang Wu and Chi-Keung Tang. [Visible Surface Reconstruction from Normals with Discontinuity Consideration](#). In *CVPR*, 2006. 1, 2
- [33] Wuyuan Xie, Miaohui Wang, Mingqiang Wei, Jianmin Jiang, and Jing Qin. [Surface Reconstruction From Normals: A Robust DGP-Based Discontinuity Preservation Approach](#). In *CVPR*, 2019. 1, 2
- [34] Dizhong Zhu and William A. P. Smith. [Least Squares Surface Reconstruction on Arbitrary Domains](#). In *ECCV*, 2020. 2

Supplementary Material

The Supplementary Material is organized as follows. In Appendix A, we derive the mathematical formulation at the core of our method. In Appendix B, we provide a novel analysis of the multiplicative factor $\gamma_{b \rightarrow a}$ used by BiNI [6] and extended in our method, and provide important insights on its effect on convergence. Appendix C provides additional insights on the positivity of the log term in our formulation ((15) in the main paper), including a mathematical proof that this property is preserved throughout the optimization, and discusses corner cases. In Appendix D, we study the impact of the choice of the ray direction vector $\boldsymbol{\tau}_m$, that controls our local planarity assumption. In Appendix E, we study the effect of the discontinuity activation term $\beta_{b \rightarrow a}^{(t)}$ in our formulation. Appendix F presents an ablation on different pixel connectivity. Appendix G presents an evaluation of the formulation accuracy with metrics in addition to the one introduced in Sec. 4.2. Appendix H provides results of our method under noisy input normals. Finally, Appendix I discusses the limitations of our method.

A. Derivation of our formulation

In the following Section, we provide a derivation of the coefficients (3) of our formulation (2). Rearranging the equations in the system (1) emerging from our local planarity assumption and using $x_b = \tau_{x_b} z_b$, $y_b = \tau_{y_b} z_b$ (by definition of τ_{x_b} , τ_{y_b}) yields the following linear system in the variables dx_{ma} , dy_{ma} , dz_{ma} , dx_{mb} , dy_{mb} , dz_{mb} :

$$\mathbf{C} \cdot \begin{bmatrix} dx_{ma} \\ dy_{ma} \\ dz_{ma} \\ dx_{mb} \\ dy_{mb} \\ dz_{mb} \end{bmatrix} = \mathbf{d}, \quad (17)$$

where

$$\mathbf{C} = \begin{bmatrix} 0 & 0 & 0 & 1 & 0 & -\tau_{x_m} \\ 0 & 0 & 0 & 0 & 1 & -\tau_{y_m} \\ -1 & 0 & \tau_{x_a} & 1 & 0 & -\tau_{x_a} \\ 0 & -1 & \tau_{y_a} & 0 & 1 & -\tau_{y_a} \\ 0 & 0 & 0 & n_{bx} & n_{by} & n_{bz} \\ n_{ax} & n_{ay} & n_{az} & 0 & 0 & 0 \end{bmatrix}, \text{ and} \quad (18)$$

$$\mathbf{d} = \begin{bmatrix} (\tau_{x_m} - \tau_{x_b})z_b \\ (\tau_{y_m} - \tau_{y_b})z_b \\ (\tau_{x_a} - \tau_{x_b})z_b \\ (\tau_{y_a} - \tau_{y_b})z_b \\ 0 \\ -n_{az}\varepsilon_{b \rightarrow a} \end{bmatrix}.$$

Solving (17) yields the following expressions for dz_{ma}

and dz_{mb} :

$$\begin{aligned} dz_{ma} &= \frac{-n_{az}}{\mathbf{n}_a^\top \boldsymbol{\tau}_a} \cdot \varepsilon_{b \rightarrow a} + \\ &\quad \frac{(n_{ax}\tau_{x_a} + n_{ay}\tau_{y_a} - n_{ax}\tau_{x_m} - n_{ay}\tau_{y_m}) \cdot \mathbf{n}_b^\top \boldsymbol{\tau}_b}{\mathbf{n}_a^\top \boldsymbol{\tau}_a \cdot \mathbf{n}_b^\top \boldsymbol{\tau}_m} \cdot z_b \\ &= \frac{-n_{az}}{\mathbf{n}_a^\top \boldsymbol{\tau}_a} \cdot \varepsilon_{b \rightarrow a} + \frac{(\mathbf{n}_a^\top \boldsymbol{\tau}_a - \mathbf{n}_a^\top \boldsymbol{\tau}_m) \cdot \mathbf{n}_b^\top \boldsymbol{\tau}_b}{\mathbf{n}_a^\top \boldsymbol{\tau}_a \cdot \mathbf{n}_b^\top \boldsymbol{\tau}_m} \cdot z_b, \\ dz_{mb} &= \frac{n_{bx}\tau_{x_b} + n_{by}\tau_{y_b} - n_{bx}\tau_{x_m} - n_{by}\tau_{y_m}}{\mathbf{n}_b^\top \boldsymbol{\tau}_m} \cdot z_b \\ &= \frac{\mathbf{n}_a^\top \boldsymbol{\tau}_a \cdot (\mathbf{n}_b^\top \boldsymbol{\tau}_b - \mathbf{n}_b^\top \boldsymbol{\tau}_m)}{\mathbf{n}_a^\top \boldsymbol{\tau}_a \cdot \mathbf{n}_b^\top \boldsymbol{\tau}_m} \cdot z_b. \end{aligned} \quad (19)$$

The final step to obtain our formulation (2), (3) follows from writing:

$$\begin{aligned} z_a &= z_b + dz_{mb} - dz_{ma} \\ &= \frac{\mathbf{n}_a^\top \boldsymbol{\tau}_a \cdot \mathbf{n}_b^\top \boldsymbol{\tau}_m}{\mathbf{n}_a^\top \boldsymbol{\tau}_a \cdot \mathbf{n}_b^\top \boldsymbol{\tau}_m} \cdot z_b + \\ &\quad \frac{\mathbf{n}_a^\top \boldsymbol{\tau}_a \cdot (\mathbf{n}_b^\top \boldsymbol{\tau}_b - \mathbf{n}_b^\top \boldsymbol{\tau}_m)}{\mathbf{n}_a^\top \boldsymbol{\tau}_a \cdot \mathbf{n}_b^\top \boldsymbol{\tau}_m} \cdot z_b + \\ &\quad - \frac{(\mathbf{n}_a^\top \boldsymbol{\tau}_a - \mathbf{n}_a^\top \boldsymbol{\tau}_m) \cdot \mathbf{n}_b^\top \boldsymbol{\tau}_b}{\mathbf{n}_a^\top \boldsymbol{\tau}_a \cdot \mathbf{n}_b^\top \boldsymbol{\tau}_m} \cdot z_b + \\ &\quad \frac{n_{az}}{\mathbf{n}_a^\top \boldsymbol{\tau}_a} \cdot \varepsilon_{b \rightarrow a} \\ &= \frac{n_{az}}{\mathbf{n}_a^\top \boldsymbol{\tau}_a} \cdot \varepsilon_{b \rightarrow a} + \frac{\mathbf{n}_a^\top \boldsymbol{\tau}_m \cdot \mathbf{n}_b^\top \boldsymbol{\tau}_b}{\mathbf{n}_a^\top \boldsymbol{\tau}_a \cdot \mathbf{n}_b^\top \boldsymbol{\tau}_m} \cdot z_b. \end{aligned} \quad (20)$$

B. Influence of the multiplicative factor $\gamma_{b \rightarrow a}$

As noted in Sec. 2 of the Supplementary Material of BiNI [8], the coefficient $\gamma_{b \rightarrow a}$ ¹, which we extend in our formulation, is crucial to achieving optimal convergence during optimization. In particular, their formulation based on the functional $\gamma_{b \rightarrow a}(\tilde{z}_a - \tilde{z}_b) = \delta_{b \rightarrow a}$ ((8) in the main paper) performs significantly better than the one derived from the equivalent equation $\tilde{z}_a - \tilde{z}_b = \delta_{b \rightarrow a} / \gamma_{b \rightarrow a}$. Similarly, we find that our formulation $\gamma_{b \rightarrow a}(\tilde{z}_a - \tilde{z}_b) = \gamma_{b \rightarrow a} \log(\omega_{b \rightarrow a} + \omega_{\varepsilon_a} \cdot \alpha_{b \rightarrow a})$ ((11) in the main paper) achieves significantly better convergence than the equivalent $\tilde{z}_a - \tilde{z}_b = \log(\omega_{b \rightarrow a} + \omega_{\varepsilon_a} \cdot \alpha_{b \rightarrow a})$.

In the following, we provide below a novel analysis of this phenomenon in light of our generic formulation based on ray direction vectors, which allows rewriting $\gamma_{b \rightarrow a}$ as

$$\gamma_{b \rightarrow a} = f \cdot \mathbf{n}_a^\top \boldsymbol{\tau}_a, \quad (21)$$

where f is the (fixed) focal length, which we generalize to the (pixel-pair specific) factor $\|\mathbf{u}_b - \mathbf{u}_a\| / \|\boldsymbol{\tau}_b - \boldsymbol{\tau}_a\|^2$. All the supporting experiments in this Section are run on the

¹Denoted as \tilde{n}_z in [8].

²Note that for an ideal pinhole camera with $f = f_x = f_y$ one has $\|\mathbf{u}_b - \mathbf{u}_a\| = \|(u_b - u_a, v_b - v_a)\|$ and $\|\boldsymbol{\tau}_b - \boldsymbol{\tau}_a\| = \|((u_b - u_a)/f, (v_b - v_a)/f, 0)\| = \|\mathbf{u}_b - \mathbf{u}_a\|/f$, from which one recovers $\|\mathbf{u}_b - \mathbf{u}_a\| / \|\boldsymbol{\tau}_b - \boldsymbol{\tau}_a\| = f$.

DiLiGenT benchmark, for 1200 iterations and for simplicity using our version without $\alpha_{b \rightarrow a}$ computation.

We start by noting that, for each pixel pair (a, b) , the coefficient $\gamma_{b \rightarrow a}$ has two effects on the optimization:

- **Effect 1 (weighting):** On one side, it introduces a quadratic factor $\gamma_{b \rightarrow a}^2$ in the corresponding term of the optimization cost function $(\tilde{\mathbf{A}}\tilde{\mathbf{z}} - \tilde{\mathbf{b}})^\top \tilde{\mathbf{W}}(\tilde{\mathbf{A}}\tilde{\mathbf{z}} - \tilde{\mathbf{b}})$ (cf. (5) in the main paper), or equivalently in its associated normal equation $\tilde{\mathbf{A}}^\top \tilde{\mathbf{W}} \tilde{\mathbf{A}} \tilde{\mathbf{z}} = \tilde{\mathbf{A}}^\top \tilde{\mathbf{W}} \tilde{\mathbf{b}}$, since both the rows of $\tilde{\mathbf{A}}$ and the corresponding elements of $\tilde{\mathbf{b}}$ are scaled by a factor $\gamma_{b \rightarrow a}$ (cf. (8) and (11) in the main paper). In other words, the optimization cost function reads as

$$(\tilde{\mathbf{A}}\tilde{\mathbf{z}} - \tilde{\mathbf{b}})^\top \tilde{\mathbf{W}}(\tilde{\mathbf{A}}\tilde{\mathbf{z}} - \tilde{\mathbf{b}}) = \sum_{(a,b)} w_{b \rightarrow a}^{\text{BiNI}} \cdot \gamma_{b \rightarrow a}^2 \cdot (\tilde{z}_a - \tilde{z}_b - \text{RHS})^2, \quad (22)$$

where RHS is $\delta_{b \rightarrow a} / \gamma_{b \rightarrow a}$ for BiNI and $\log(\omega_{b \rightarrow a} + \omega_{\varepsilon_a} \cdot \alpha_{b \rightarrow a})$ for Ours. Therefore, each residual is effectively scaled by $w_{b \rightarrow a}^{\text{BiNI}} \cdot \gamma_{b \rightarrow a}^2$ rather than only by $w_{b \rightarrow a}^{\text{BiNI}}$.

- **Effect 2 (sharpness of the bilateral weights):** On the other side, it impacts the magnitude of the bilateral weights $w_{b \rightarrow a}^{\text{BiNI}} = \sigma_k(\text{res}_{-b \rightarrow a}^2 - \text{res}_{b \rightarrow a}^2)$, where $\text{res}_{b \rightarrow a} := \gamma_{b \rightarrow a}(\tilde{z}_a - \tilde{z}_b)$ (see also (10) in the main paper). Since from (21) $\gamma_{b \rightarrow a} \approx \gamma_{-b \rightarrow a}$, with exact equality when f is constant, it follows that

$$\begin{aligned} w_{b \rightarrow a}^{\text{BiNI}} &= \sigma_k(\gamma_{b \rightarrow a}^2 \cdot ((\tilde{z}_a - \tilde{z}_b)^2 - (\tilde{z}_a - \tilde{z}_{-b})^2)) \\ &= \sigma_{k \cdot \gamma_{b \rightarrow a}^2}((\tilde{z}_a - \tilde{z}_b)^2 - (\tilde{z}_a - \tilde{z}_{-b})^2), \end{aligned} \quad (23)$$

i.e., $\gamma_{b \rightarrow a}^2$ can be subsumed into the parameter k of the sigmoid σ_k . As a consequence, $\gamma_{b \rightarrow a}$ controls the convergence of the bilateral weights, so that for fixed \tilde{z}_a and \tilde{z}_b , a larger $\gamma_{b \rightarrow a}^2$ causes smaller depth differences between the two sides to be detected as a one-sided discontinuity, and smaller values result in a less sharp convergence.

Crucially, we observe that the effects of the two terms f and $\mathbf{n}_a^\top \boldsymbol{\tau}_a$ in (21) can be decoupled and summarized in the following two Propositions:

Proposition 1: Effect of the term f

The term f acts as a constant (or near constant, in the case of $f = \|\mathbf{u}_b - \mathbf{u}_a\| / \|\boldsymbol{\tau}_b - \boldsymbol{\tau}_a\|$) that controls the sharpness of the bilateral weights $w_{b \rightarrow a}^{\text{BiNI}}$.

Proposition 2: Effect of the term $\mathbf{n}_a^\top \boldsymbol{\tau}_a$

The term $\mathbf{n}_a^\top \boldsymbol{\tau}_a$ introduces an active weighting mechanism (in addition to $w_{b \rightarrow a}^{\text{BiNI}}$) based on the collinearity between surface normals and ray directions, reducing the influence of pixel pairs close to a discontinuity.

We provide below arguments and empirical verifications supporting the above Propositions.

Argument for Proposition 1. Since f is constant (or approximately constant), it can be factored out of each term $\gamma_{b \rightarrow a}^2$ in the optimization cost function (22). Since multiplying the cost function by a constant factor does not affect its minimizing solution, it follows that the term f is not an influencing factor for Effect 1 (weighting). We verify this by running our method using $\gamma_{b \rightarrow a} = \mathbf{n}_a^\top \boldsymbol{\tau}_a$ in our cost function (22) and $\gamma_{b \rightarrow a} = f \cdot \mathbf{n}_a^\top \boldsymbol{\tau}_a$ in the bilateral weights (23). As expected, up to minimal differences that we attribute to machine precision, the results match those obtained when using the full factor $\gamma_{b \rightarrow a} = f \cdot \mathbf{n}_a^\top \boldsymbol{\tau}_a$ in the cost function (cf. first and second row in Tab. 3).

We verify that instead the term f does indeed contribute to Effect 2 (sharpness of the bilateral weights) by varying its value in the $\gamma_{b \rightarrow a}$ factor of the bilateral weights, while maintaining a fixed $\gamma_{b \rightarrow a} = \mathbf{n}_a^\top \boldsymbol{\tau}_a$ in our cost function. Comparing rows 2 to 5 in Tab. 3 shows that indeed different values of f result in different convergence; while the change is object-specific, the main emerging trend appears to indicate that worse convergence is obtained for lower values of f , which correspond to a less sharp sigmoid.

Argument for Proposition 2. Since unlike f the term $\mathbf{n}_a^\top \boldsymbol{\tau}_a$ is highly pixel specific, it is not possible to find a single constant that can be absorbed into the parameter k of the sigmoid. It is therefore not straightforward to draw conclusions about its contribution to Effect 2 (sharpness of the bilateral weights). We can however verify that the term $\mathbf{n}_a^\top \boldsymbol{\tau}_a$ has a strong influence on Effect 1 (weighting), by removing it from the $\gamma_{b \rightarrow a}$ factor of the cost function (which is therefore set to f), while maintaining it in $\gamma_{b \rightarrow a}$ in the bilateral weights. Comparing the last and the first row of Tab. 3 confirms that the accuracy of the reconstruction dramatically decreases when the term does not contribute to the cost function, which indicates that it plays an active role in determining the convergence of the optimization, by introducing equation-specific weights. Interestingly, as we previously observed in Sec. 3.1, the term $\mathbf{n}_a^\top \boldsymbol{\tau}_a$ strongly correlates with surface discontinuities, with pixels close to object boundaries or local discontinuities attaining a small value for this term. More generally, as evident from its dot-product definition, the term $\mathbf{n}_a^\top \boldsymbol{\tau}_a$ encodes the degree of collinearity between surface normal and the ray direction vector at each pixel (cf. Fig. 8 for a visualization). As a consequence, its effect over the optimization is to balance the influence of the residuals, decreasing the weight of errors close to discontinuities, while increasing the influence of residuals at points where the camera rays hit the surface at a close-to-right angle.



Figure 8. **Visualization of the terms $|\mathbf{n}_a^\top \boldsymbol{\tau}_a|$, DiLiGenT dataset [28].** The terms encode the degree of collinearity between the surface normals and the ray direction vectors. Low values are attained at pixels where the ray direction vector is perpendicular to the surface normal, a necessary condition for the corresponding point to lie on the object boundary.

Value of $\gamma_{b \rightarrow a}$		bear	buddha	cat	cow	harvest	pot1	pot2	reading	goblet
Cost function (22)	$w_{b \rightarrow a}^{\text{BiNI}}$ (23)									
$f \cdot \mathbf{n}_a^\top \boldsymbol{\tau}_a$	$f \cdot \mathbf{n}_a^\top \boldsymbol{\tau}_a$	0.07	0.26	0.06	0.08	5.54	0.49	0.13	0.11	6.33
$\mathbf{n}_a^\top \boldsymbol{\tau}_a$	$f \cdot \mathbf{n}_a^\top \boldsymbol{\tau}_a$	0.07	0.25	0.06	0.08	5.33	0.49	0.13	0.12	6.60
$\mathbf{n}_a^\top \boldsymbol{\tau}_a$	$3000 \cdot \mathbf{n}_a^\top \boldsymbol{\tau}_a$	0.09	0.27	0.11	0.09	3.89	0.47	0.15	0.12	7.96
$\mathbf{n}_a^\top \boldsymbol{\tau}_a$	$2000 \cdot \mathbf{n}_a^\top \boldsymbol{\tau}_a$	0.06	0.98	0.17	0.18	1.71	0.48	0.25	0.27	8.63
$\mathbf{n}_a^\top \boldsymbol{\tau}_a$	$1000 \cdot \mathbf{n}_a^\top \boldsymbol{\tau}_a$	0.04	1.41	0.08	0.30	2.51	0.72	0.28	1.19	9.46
f	$f \cdot \mathbf{n}_a^\top \boldsymbol{\tau}_a$	0.48	2.53	0.69	0.39	4.84	14.40	0.42	3.16	10.28

Table 3. **Ablation on the terms in $\gamma_{b \rightarrow a}$, DiLiGenT dataset [28].** For each experiment, we report the mean absolute depth error (MADE) [mm]. All experiments are without $\alpha_{b \rightarrow a}$ computation, $k = 2$ for $w_{b \rightarrow a}^{(t)}$ (as default), and are run for 1200 iterations. Where used, f denotes $\|\mathbf{u}_b - \mathbf{u}_a\| / \|\boldsymbol{\tau}_b - \boldsymbol{\tau}_a\|$. For reference, the values of f_x and f_y in the dataset are $f_x \approx 3772.1$ [px] and $f_y \approx 3759.0$ [px].

C. Analysis of the positivity of the log term

In this Section we provide further insights on the positivity of the log term in our formulation ((15) in the main paper).

We start by empirically verifying that, for our choice $\boldsymbol{\tau}_m = (\boldsymbol{\tau}_a + \boldsymbol{\tau}_b)/2$, the terms $\mathbf{n}_a^\top \boldsymbol{\tau}_m$ and $\mathbf{n}_b^\top \boldsymbol{\tau}_m$ are both strictly positive for all but a single pixel (object `pot1`) across all the objects in the DiLiGenT dataset, used for our main experiments. Furthermore, also for this outlier pixel, the effects of the two pixels cancel out and the corresponding term $\omega_{b \rightarrow a} = (\mathbf{n}_a^\top \boldsymbol{\tau}_m \cdot \mathbf{n}_b^\top \boldsymbol{\tau}_b) / (\mathbf{n}_a^\top \boldsymbol{\tau}_a \cdot \mathbf{n}_b^\top \boldsymbol{\tau}_m)$ is strictly positive, leading to a positive log term at all pixels in the first iteration of our optimization.

We now briefly analyze under which conditions we can expect an outlier, negative $\omega_{b \rightarrow a}$ term. Since, as noted in Sec. 3.1, for physically meaningful normals (*i.e.*, corresponding to observable surface points) the positivity of $\omega_{b \rightarrow a}$ reduces to the positivity of $\mathbf{n}_a^\top \boldsymbol{\tau}_m$ and $\mathbf{n}_b^\top \boldsymbol{\tau}_m$, we can focus on the case where the latter two terms have opposite signs. Figure 9 provides an illustration of an instance in which such a corner case may arise. In the depicted setting, the surface has low inclination relative to the camera on the side of point \mathbf{p}_a , but large inclination on the side of point \mathbf{p}_b . As consequence, on the side of \mathbf{p}_a both the angles between \mathbf{n}_a and $\boldsymbol{\tau}_a$ and between \mathbf{n}_a and $\boldsymbol{\tau}_m$ are significantly larger than 90° , *i.e.* $\mathbf{n}_a^\top \boldsymbol{\tau}_a < 0$ and $\mathbf{n}_a^\top \boldsymbol{\tau}_m < 0$. On the opposite side, however, the angle between \mathbf{n}_b and $\boldsymbol{\tau}_b$ is only slightly larger than 90° (hence $\mathbf{n}_b^\top \boldsymbol{\tau}_b \approx 0$, but still negative), while the angle between \mathbf{n}_b and $\boldsymbol{\tau}_m$ is smaller than 90° , causing $\mathbf{n}_b^\top \boldsymbol{\tau}_m$ to be positive and therefore $\omega_{b \rightarrow a}$ to be negative. While such outlier cases might indeed arise, it is

possible to detect and handle them, for instance by excluding the corresponding equation from the optimization or by choosing a different value of $\boldsymbol{\tau}_m$ (*cf.* Appendix D). Furthermore, their occurrence is unlikely in practice, since the sign flipping between $\mathbf{n}_b^\top \boldsymbol{\tau}_b$ and $\mathbf{n}_b^\top \boldsymbol{\tau}_m$ would need to occur within a very limited angular space: as a reference, using $\boldsymbol{\tau}_m = (\boldsymbol{\tau}_a + \boldsymbol{\tau}_b)/2$, the angle between $\boldsymbol{\tau}_m$ and $\boldsymbol{\tau}_b$ is approximately $\frac{1}{2} \arctan\left(\frac{1 \text{ px}}{3700 \text{ px}}\right) \approx 0.008^\circ$ in the DiLiGenT dataset, for which $f_x \approx 3772.1$ px and $f_y \approx 3759.0$ px.

Assuming $\omega_{b \rightarrow a} > 0$, hence that the argument of the log term in (15) is positive in the first optimization iteration, it is straightforward to show that the argument also stays positive throughout the optimization, as we prove below.

From (14) in the main paper, $\omega_{b \rightarrow a} + \omega_{\varepsilon_a} \cdot \alpha_{b \rightarrow a}^{(t+1)} = \exp\left(\tilde{z}_a^{(t)} - \tilde{z}_b^{(t)}\right)$. Since the exponential function is bijective and defined anywhere in \mathbb{R} , it follows that for any value of $\tilde{z}_a^{(t)}$ and $\tilde{z}_b^{(t)}$ a corresponding value for the term $\omega_{b \rightarrow a} + \omega_{\varepsilon_a} \cdot \alpha_{b \rightarrow a}^{(t+1)}$ can be found and thereby of $\alpha_{b \rightarrow a}^{(t+1)}$ (provided that $\omega_{\varepsilon_a} \neq 0$, *i.e.*, from (3) $n_{a_z} \neq 0$, which is always the case because $n_{a_z} = 0$ corresponds to a surface perpendicular to the image plane). Since the exponential function has strictly positive codomain, it also follows that for all t 's:

$$\omega_{b \rightarrow a} + \omega_{\varepsilon_a} \cdot \alpha_{b \rightarrow a}^{(t+1)} > 0. \quad (24)$$

From $\omega_{b \rightarrow a} > 0$ and (24) and since $\beta_{b \rightarrow a}^{(t)} \in [0, 1]$ by design, it follows that $\omega_{b \rightarrow a} + \omega_{\varepsilon_a} \cdot \alpha_{b \rightarrow a}^{(t)} \cdot \beta_{b \rightarrow a}^{(t)} > 0$, which proves the hypothesis. Indeed:

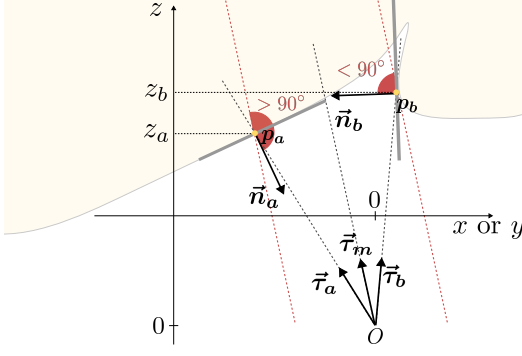


Figure 9. **Visualization of a corner case in our local planarity assumption in 3D.** For the chosen configuration, the ray direction vector τ_m forms an angle smaller than 90° with \mathbf{n}_b and larger than 90° with \mathbf{n}_a , resulting in $\mathbf{n}_a^\top \tau_m < 0$ and $\mathbf{n}_b^\top \tau_m > 0$.

- If $\omega_{\varepsilon_a} \cdot \alpha_{b \rightarrow a}^{(t)} \geq 0$, one has

$$\begin{aligned} \omega_{\varepsilon_a} \cdot \alpha_{b \rightarrow a}^{(t)} \cdot \beta_{b \rightarrow a}^{(t)} &\geq 0 & (\beta_{b \rightarrow a}^{(t)} \geq 0) \\ \Rightarrow \omega_{b \rightarrow a} + \omega_{\varepsilon_a} \cdot \alpha_{b \rightarrow a}^{(t)} \cdot \beta_{b \rightarrow a}^{(t)} &\geq \omega_{b \rightarrow a} & (\omega_{b \rightarrow a} \in \mathbb{R}) \\ \Rightarrow \omega_{b \rightarrow a} + \omega_{\varepsilon_a} \cdot \alpha_{b \rightarrow a}^{(t)} \cdot \beta_{b \rightarrow a}^{(t)} &> 0; & (\omega_{b \rightarrow a} > 0) \end{aligned}$$

- If $\omega_{\varepsilon_a} \cdot \alpha_{b \rightarrow a}^{(t)} < 0$, it follows that

$$\begin{aligned} \omega_{\varepsilon_a} \cdot \alpha_{b \rightarrow a}^{(t)} \cdot \beta_{b \rightarrow a}^{(t)} &\geq \omega_{\varepsilon_a} \cdot \alpha_{b \rightarrow a}^{(t)} & (\beta_{b \rightarrow a}^{(t)} \in [0, 1]) \\ \Rightarrow \omega_{b \rightarrow a} + \omega_{\varepsilon_a} \cdot \alpha_{b \rightarrow a}^{(t)} \cdot \beta_{b \rightarrow a}^{(t)} &\geq & \\ &\omega_{b \rightarrow a} + \omega_{\varepsilon_a} \cdot \alpha_{b \rightarrow a}^{(t)} & (\omega_{b \rightarrow a} > 0) \\ \Rightarrow \omega_{b \rightarrow a} + \omega_{\varepsilon_a} \cdot \alpha_{b \rightarrow a}^{(t)} \cdot \beta_{b \rightarrow a}^{(t)} &> 0. & (\text{from (24)}) \end{aligned}$$

D. Impact of the choice of τ_m

In the following Section, we provide an ablation on the choice of τ_m , which controls the planar assumption of our method (*cf.* Fig. 9 and Fig. 2 in the main paper).

As mentioned in Sec. 3.1 in the main paper, τ_m can be parametrized as interpolating between τ_a and τ_b , *i.e.*, $\tau_m = \tau_a + \lambda_m(\tau_b - \tau_a)$, with $\lambda_m \in [0, 1]$. A natural choice, which we adopt in our main experiments, is to orient τ_m at an equal angular distance from τ_a and τ_b , *i.e.* setting $\lambda_m = 0.5$ uniformly for all pixels. However, we note that in certain settings a pixel-pair-specific choice $\lambda_{m,b \rightarrow a} : \tau_m = \tau_a + \lambda_{m,b \rightarrow a}(\tau_b - \tau_a)$ might be desirable. An argument in favor of this point is for instance shown through a corner case similar to that considered in Appendix C (Fig. 10), in which on one of the two sides (the side of p_b in Fig. 10) the surface has a significantly larger inclination relative to the camera. As a consequence, as exemplified by Fig. 10, our planar assumption holds more accurately if τ_m is oriented closer to the side with the larger inclination, in which case a smaller discontinuity term $|\varepsilon_{b \rightarrow a}|$ is obtained. Since, as mentioned in Appendix B, the quantity $\mathbf{n}_a^\top \tau_a$ naturally encodes surface orientation with respect to the camera, the condition

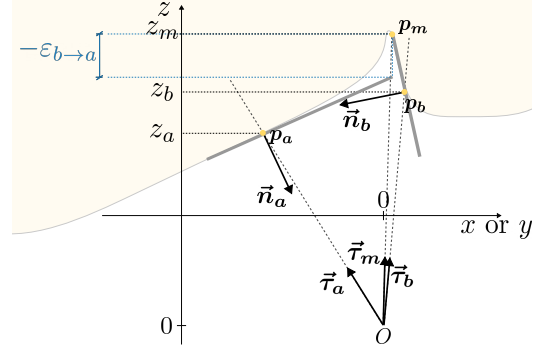


Figure 10. **Visualization of an adaptive strategy for τ_m .** If the surface has a large inclination relative to the camera on one of the two sides (here the side of p_b , hence $|\mathbf{n}_b^\top \tau_b| \ll |\mathbf{n}_a^\top \tau_a|$), orienting τ_m closer to the latter side yields a smaller $|\varepsilon_{b \rightarrow a}|$.

of unbalanced inclination between the two sides can also be expressed as $|\mathbf{n}_b^\top \tau_b| \ll |\mathbf{n}_a^\top \tau_a|$. In this ablation, we additionally consider the quantity n_{az} , which similarly to $\mathbf{n}_a^\top \tau_a$ attains a low value in proximity to discontinuities.

We note that the interpolating function $\lambda_{m,b \rightarrow a}$ needs to be such that τ_m intersects the same surface point p_m both in the direction $b \rightarrow a$ (*i.e.*, when considering b a neighbor of a) and in the direction $a \rightarrow b$ (*i.e.*, when considering a a neighbor of b). This can be expressed mathematically by the condition $\lambda_{m,b \rightarrow a} = 1 - \lambda_{m,a \rightarrow b}$. We note that the sigmoid function naturally fulfills this condition when composed with an even function, and we therefore set in this ablation $\lambda_{m,b \rightarrow a} = \sigma_{k_m}(f(a, b))$, with different values for k_m , and with $f(a, b)$ either $(\mathbf{n}_a^\top \tau_a)^2 - (\mathbf{n}_b^\top \tau_b)^2$, $n_{az}^2 - n_{bz}^2$, or $(n_{az} \cdot \mathbf{n}_a^\top \tau_a)^2 - (n_{bz} \cdot \mathbf{n}_b^\top \tau_b)^2$.

Table 4 shows the results of this ablation, which we perform on the DiLiGenT dataset. For most objects, introducing a pixel-specific λ_m results generally in lower reconstruction accuracy using any of the functions $f(a, b)$ listed above; larger values of k_m (hence more sharply weighting inclination differences between the two sides) further decrease the performance. A noticeable exception is represented by the two objects with larger discontinuities (harvest and goblet), for which specific choices of parameters can lead to improved reconstruction accuracy.

E. Impact of the discontinuity activation term

In this Section, we provide an ablation analysis on the impact of our discontinuity activation term $\beta_{b \rightarrow a}^{(t)}$ on the reconstruction accuracy. Table 5 reports the mean absolute depth error on the DiLiGenT dataset as we vary the hyperparameters q and ρ (*cf.* (16) in the main paper), the effect of which can be visualized in Fig. 11. For $\rho = 0.25$, the results show object-specific trends, with some objects achieving higher accuracy for sharper changes of $\beta_{b \rightarrow a}^{(t)}$ (larger q , for instance harvest, pot1, reading) and others

λ_m	k_m	bear	buddha	cat	cow	harvest	pot1	pot2	reading	goblet
0.5	N/A	0.07	0.26	0.06	0.08	4.83	0.50	0.13	0.12	6.56
$\sigma_{k_m} ((\mathbf{n}_a^\top \boldsymbol{\tau}_a)^2 - (\mathbf{n}_b^\top \boldsymbol{\tau}_b)^2)$	1	0.15	0.33	0.09	0.12	5.12	0.52	0.17	0.19	5.73
	2	0.22	0.72	0.13	0.16	2.45	0.53	0.22	0.29	6.23
	3	0.29	1.40	0.16	0.19	3.66	0.56	0.30	0.38	6.11
$\sigma_{k_m} (n_{az}^2 - n_{bz}^2)$	1	0.15	0.33	0.09	0.12	4.65	0.50	0.17	0.19	5.69
	2	0.22	0.71	0.13	0.16	2.51	0.53	0.22	0.28	6.12
	3	0.29	1.42	0.16	0.19	5.49	0.56	0.30	0.38	6.06
$\sigma_{k_m} ((n_{az} \cdot \mathbf{n}_a^\top \boldsymbol{\tau}_a)^2 - (n_{bz} \cdot \mathbf{n}_b^\top \boldsymbol{\tau}_b)^2)$	1	0.11	0.25	0.08	0.11	4.95	0.51	0.16	0.15	5.38
	2	0.15	0.45	0.10	0.13	2.73	0.52	0.20	0.20	5.40
	3	0.19	1.03	0.13	0.16	2.74	0.55	0.24	0.39	5.61

Table 4. Mean absolute depth error (MADE) [mm] on the DiLiGenT benchmark [28] for different choices of λ_m , where $\boldsymbol{\tau}_m = \boldsymbol{\tau}_a + \lambda_m(\boldsymbol{\tau}_b - \boldsymbol{\tau}_a)$. All the experiments are run for 1200 iterations with $\alpha_{b \rightarrow a} = 0$. σ_{k_m} denotes the sigmoid function $\sigma_{k_m}(x) = 1/(1 + \exp(-k_m \cdot x))$.

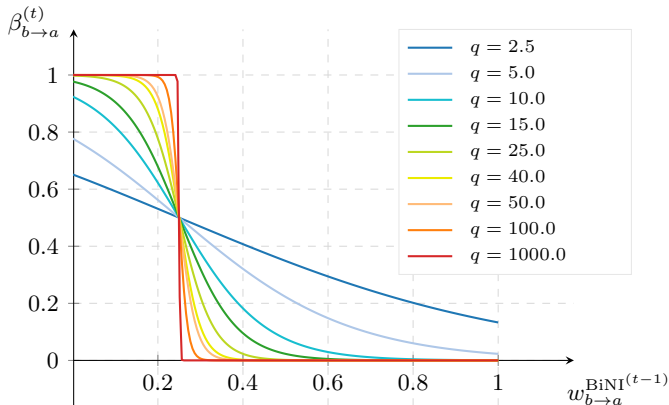


Figure 11. Discontinuity activation term (16) for $\rho = 0.25$ and different values of q . For $\rho = 0.5$, the plots are shifted to the right by 0.25 units along the $w_{b \rightarrow a}^{\text{BiNI}^{(t-1)}}$ axis. Cf. Tab. 5 for a quantitative evaluation on the effect of the parameters ρ and q .

favoring a smoother discontinuity activation term (smaller q , for instance bear, pot2). For $\rho = 0.5$, the method achieves worse accuracy, in most instances also lower than the version without computation of $\alpha_{b \rightarrow a}$ (cf. Tab. 2 in the main paper). This performance drop is expected, since for $\rho = 0.5$ the discontinuity term significantly deviates from its designed objective, namely that it should tend smoothly to zero as $w_{b \rightarrow a}^{\text{BiNI}^{(t-1)}} \rightarrow 0.5^-$ and smoothly to one as $w_{b \rightarrow a}^{\text{BiNI}^{(t-1)}} \rightarrow 0.5^+$ (cf. Sec. 3.3 in the main paper for a detailed explanation of this design choice).

F. Impact of the connectivity

Since our method allows using pixel connectivities not limited to standard 4-connectivity, in this Section we investigate whether using alternative connectivities can yield improved reconstruction accuracy. Table 6 shows the results of this ablation, where we test our method on the DiLiGenT dataset using standard 4-connectivity (as in the main paper), 4-connectivity defined along the diagonals

rather than the horizontal and vertical direction, and full 8-connectivity. While 4-connectivity along the diagonals, with very limited exceptions, generally results in significantly worse performance, we note that, interestingly, full 8-connectivity produces comparable or slightly better reconstructions than standard 4-connectivity on some objects (e.g. cow, pot1, pot2). However, this improvement is contrasted by reduced accuracy on other objects (e.g. buddha, cat, reading) and reduced effect of the $\alpha_{b \rightarrow a}$ computation, leaving standard 4-connectivity as the most robust and balanced option.

G. Additional evaluations of the formulation accuracy

In Tables 7 and Tab. 8, similarly to Tab. 1 in the main paper, we provide metrics to evaluate how accurately our formulation approximates the ground-truth relation between depth and surface normals compared to previous methods. In particular, to complement the evaluation of the *absolute* accuracy from the main paper, we report here *relative* metrics, specifically the residual $|(\tilde{z}_a - \tilde{z}_b - \text{RHS} / \gamma_{b \rightarrow a}) / \tilde{z}_a|$ computed on the ground-truth log-depth map (Tab. 7) and the residual $|(z_a - \exp(\text{RHS} / \gamma_{b \rightarrow a}) \cdot z_b) / z_a|$ computed on the ground-truth depth map (Tab. 8), where RHS denotes the right-hand side of (8) for BiNI and (11) for Ours.

The results confirm the findings from the main paper. Namely, while for two objects our method has larger residual standard deviation than BiNI [6] (buddha and pot1), it achieves lower mean residual error by one or two orders of magnitude and lower standard deviation for most objects.

H. Results for noisy inputs

In this Section, we investigate the robustness of our method to noise in the input normal map.

Similarly to previous methods [8], we simulate the presence of outlier normals by replacing the original normals with randomly sampled unit vectors, with different percentages of sampled pixels. Figure 12 shows that without pre-

ρ	q	bear	buddha	cat	cow	harvest	pot1	pot2	reading	goblet
0.25	2.5	0.04	0.28	0.06	0.11	4.35	0.57	0.13	0.17	5.86
	5.0	0.02	0.22	0.22	0.09	1.11	0.53	0.12	0.14	2.43
	10.0	0.02	0.25	0.06	0.08	0.93	0.54	0.12	0.16	1.63
	15.0	0.03	0.24	0.06	0.08	0.78	0.55	0.12	0.16	1.52
	25.0	0.03	0.25	0.06	0.10	0.83	0.55	0.13	0.13	5.78
	40.0	0.03	0.23	0.06	0.08	0.60	0.51	0.13	0.18	6.22
	50.0	0.03	0.24	0.06	0.08	0.73	0.49	0.13	0.17	4.72
	100.0	0.03	0.23	0.06	0.08	4.01	0.48	0.14	0.17	6.21
1000.0	0.03	0.23	0.08	0.08	0.64	0.48	0.14	0.10	6.10	
0.50	2.5	0.08	0.39	0.06	0.12	2.20	0.62	0.14	0.20	5.98
	5.0	0.09	0.47	0.09	0.12	3.40	0.64	0.13	0.52	6.25
	10.0	0.09	0.52	0.09	0.12	1.88	0.58	0.13	0.54	6.18
	15.0	0.09	0.57	0.08	0.12	2.52	0.64	0.18	0.55	6.14
	25.0	0.09	0.67	0.08	0.12	1.10	0.63	0.17	0.73	4.62
	40.0	0.09	0.40	0.11	0.12	2.13	0.69	0.16	0.59	6.96
	50.0	0.09	0.70	0.12	0.12	2.21	0.61	0.17	0.45	7.23
	100.0	0.10	0.83	0.11	0.11	2.03	0.60	0.16	0.46	7.26
1000.0	0.10	0.70	0.14	0.11	2.58	0.87	0.16	0.51	6.94	

Table 5. Mean absolute depth error (MADE) [mm] on the DiLiGenT dataset [28] for $\rho \in \{0.25, 0.50\}$ and different values of q . For each object, **bold** denotes the best result across the experiments. All the experiments are run for 1200 iterations.

Method	Connectivity	bear	buddha	cat	cow	harvest	pot1	pot2	reading	goblet
Ours w/o $\alpha_{b \rightarrow a}$ computation	4-connectivity	0.07	0.26	0.06	0.08	4.83	0.50	0.13	0.12	6.56
	4-connectivity (diagonal)	0.26	0.39	0.30	0.09	1.68	0.47	0.15	0.26	7.31
	8-connectivity	0.06	0.35	0.29	0.09	2.56	0.36	0.12	0.39	4.44
Ours	4-connectivity	0.03	0.24	0.06	0.08	0.73	0.49	0.13	0.17	4.72
	4-connectivity (diagonal)	0.12	0.69	0.28	0.09	1.76	0.50	0.14	0.42	5.56
	8-connectivity	0.15	0.35	0.32	0.08	3.82	0.37	0.13	0.50	5.14

Table 6. Mean absolute depth error (MADE) [mm] on the DiLiGenT dataset [28] for different connectivities. For each object and method, **bold** denotes the best result across the connectivities. All the experiments are run for 1200 iterations with $\tau_m = (\tau_a + \tau_b)/2$. Ours corresponds to the hyperparameter setting of our main experiments ($q = 50.0$ and $\rho = 0.25$ in (16)).

Method	bear	buddha	cat	cow	harvest	pot1	pot2	reading	goblet
BiNI [6]	$(2.37 \pm 3.15) \times 10^{-5}$	$(3.18 \pm 8.12) \times 10^{-5}$	$(0.35 \pm 2.28) \times 10^{-4}$	$(2.65 \pm 4.32) \times 10^{-5}$	$(0.38 \pm 1.86) \times 10^{-4}$	$(2.89 \pm 6.75) \times 10^{-5}$	$(2.59 \pm 4.07) \times 10^{-5}$	$(0.36 \pm 1.03) \times 10^{-4}$	$(0.32 \pm 1.01) \times 10^{-4}$
Ours	$(0.08 \pm 1.25) \times 10^{-5}$	$(0.09 \pm 1.47) \times 10^{-4}$	$(0.04 \pm 2.48) \times 10^{-4}$	$(0.18 \pm 2.64) \times 10^{-5}$	$(0.18 \pm 1.77) \times 10^{-4}$	$(0.09 \pm 6.52) \times 10^{-4}$	$(0.33 \pm 3.03) \times 10^{-5}$	$(0.78 \pm 8.88) \times 10^{-5}$	$(0.61 \pm 9.10) \times 10^{-5}$

Table 7. Relative formulation accuracy on the ground-truth log-depth map, DiLiGenT dataset [28]. For both methods, we report mean and standard deviation across the pixels of the relative residual $|(\tilde{z}_a - \tilde{z}_b - \text{RHS} / \gamma_{b \rightarrow a}) / \tilde{z}_a|$ computed on the ground-truth log-depth map, where RHS denotes the right-hand side of (8) for BiNI and (11) for Ours. We use $\tau_m = (\tau_a + \tau_b)/2$ and $\alpha_{b \rightarrow a} = 0$ for Ours.

Method	bear	buddha	cat	cow	harvest	pot1	pot2	reading	goblet
BiNI [6]	$(2.46 \pm 2.39) \times 10^{-4}$	$(2.45 \pm 5.39) \times 10^{-4}$	$(3.30 \pm 6.30) \times 10^{-4}$	$(2.35 \pm 2.89) \times 10^{-4}$	$(0.29 \pm 1.33) \times 10^{-3}$	$(2.17 \pm 4.46) \times 10^{-4}$	$(1.89 \pm 3.01) \times 10^{-4}$	$(3.59 \pm 7.21) \times 10^{-4}$	$(2.37 \pm 7.45) \times 10^{-4}$
Ours	$(0.60 \pm 9.13) \times 10^{-5}$	$(0.06 \pm 1.10) \times 10^{-3}$	$(0.03 \pm 1.87) \times 10^{-3}$	$(0.13 \pm 1.94) \times 10^{-4}$	$(0.13 \pm 1.30) \times 10^{-3}$	$(0.07 \pm 8.46) \times 10^{-3}$	$(0.25 \pm 2.22) \times 10^{-4}$	$(0.57 \pm 6.51) \times 10^{-4}$	$(0.45 \pm 6.66) \times 10^{-4}$

Table 8. Relative formulation accuracy on the ground-truth depth map, DiLiGenT dataset [28]. For both methods, we report mean and standard deviation across the pixels of the relative residual $|(z_a - \exp(\text{RHS} / \gamma_{b \rightarrow a}) \cdot z_b) / z_a|$ computed on the ground-truth depth map, where RHS denotes the right-hand side of (8) for BiNI and (11) for Ours. We use $\tau_m = (\tau_a + \tau_b)/2$ and $\alpha_{b \rightarrow a} = 0$ for Ours.

processing the normal maps, our method can reconstruct most of the underlying surface, but suffers from the presence of spike artifacts and non-smooth effects on the surface (second block from the top in Fig. 12). We note, however, that a large part of the outliers can and should be detected, because they correspond to physically impossible normals. In particular, as previously observed both in the main paper and in Appendix B, a necessary condition for the surface to be observable at one point p_a is that the dot product $\mathbf{n}_a^\top \boldsymbol{\tau}_a$

at the corresponding pixel a is negative. We observe that enforcing this condition by applying an averaging filter to the normals at pixels where $\mathbf{n}_a^\top \boldsymbol{\tau}_a > 0$ results in a reduction of the amount of spike artifacts (third block from the top in Fig. 12). We additionally note that the presence of outliers can also be detected by inspecting the distribution of $\mathbf{n}_a^\top \boldsymbol{\tau}_a$ or of its absolute value: while in a natural surface these quantities vary continuously across the surface with the exception of boundary regions, for the perturbed normal maps

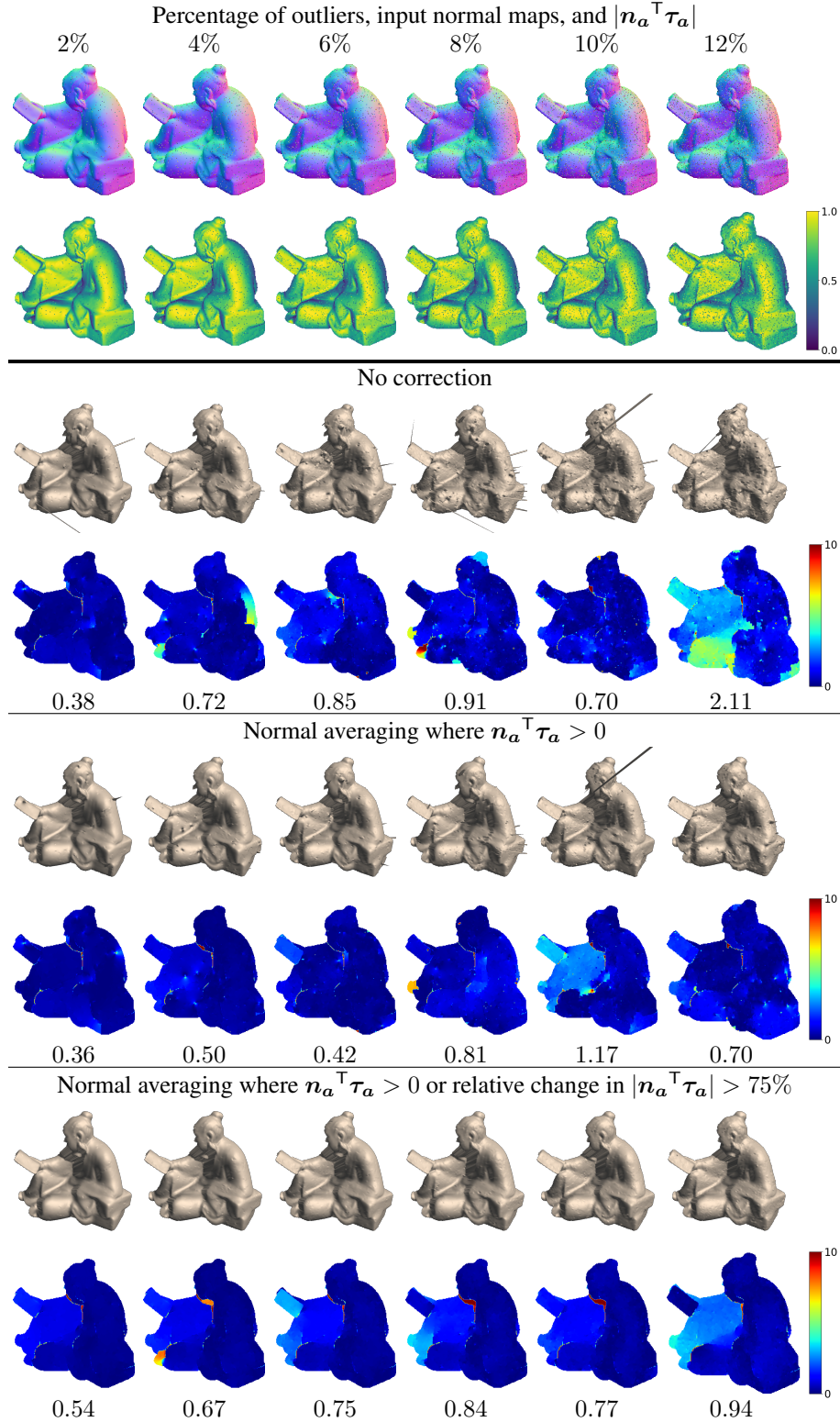


Figure 12. **Ablation on the effect of outliers, object harvest from the DiLiGenT [28] dataset.** We introduce increasing amounts of outliers, for which we replace the surface normal with a randomly sampled unit-norm vector. For each variant, we show the reconstructed surface, the corresponding absolute depth error map, and its mean value (MADE, in mm).

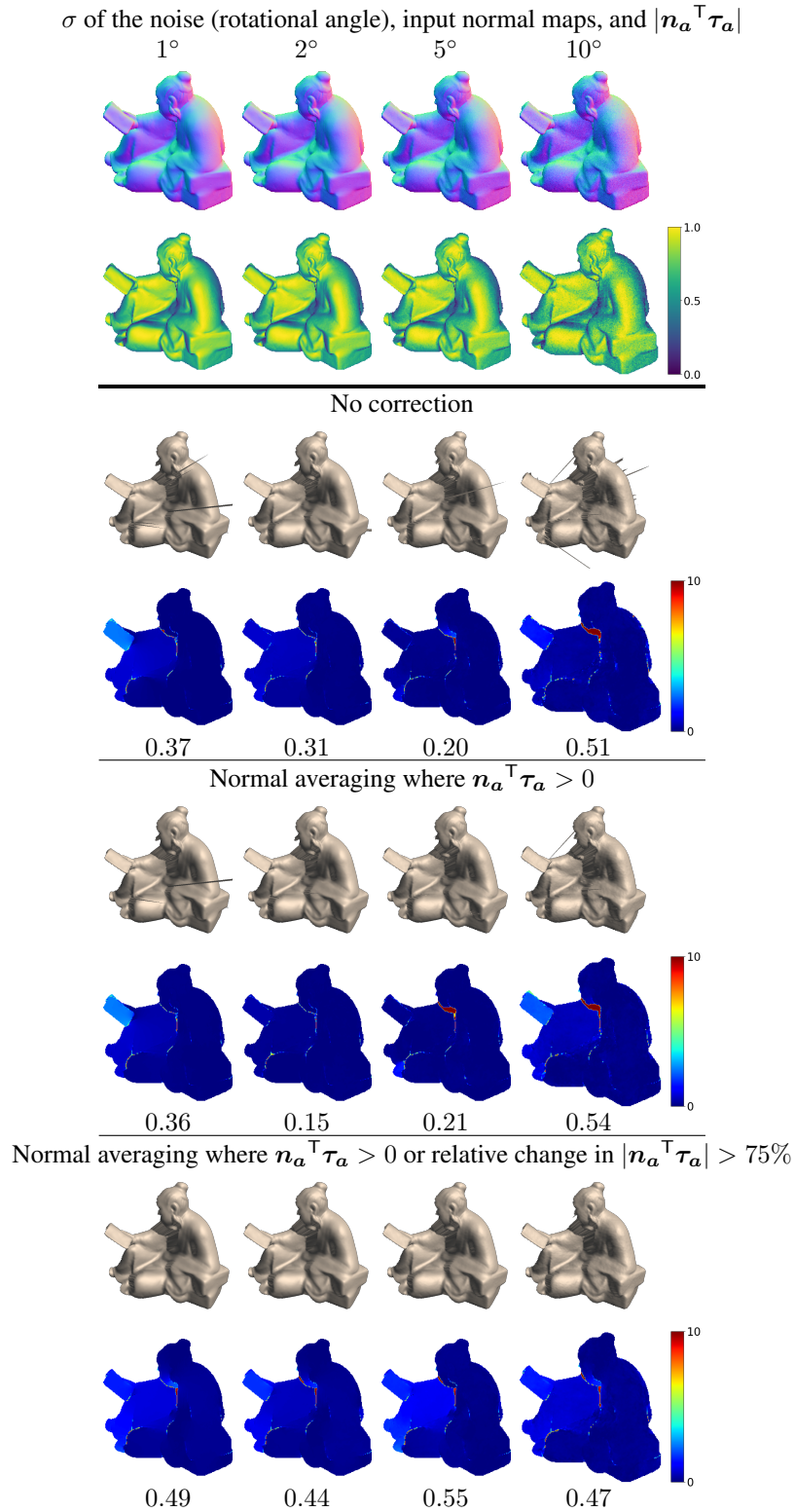


Figure 13. **Ablation on the effect of rotational noise, object harvest from the DiLiGenT [28] dataset.** We perturb the surface normals at each pixel, rotating them around randomly sampled axes by angles sampled from Gaussian distributions with increasingly larger standard deviations. For each variant, we show the reconstructed surface, the corresponding absolute depth error map, and its mean value (MADE, in mm).

salt-and-pepper noise can be observed in correspondence to the outliers (*cf.* second row in the top block of Fig. 12). We verify that applying average filtering also to pixels where $|\mathbf{n}_a^\top \boldsymbol{\tau}_a|$ deviates significantly from the mean value in its neighborhood further mitigates the effect of the outliers, removing spike artifacts and recovering the smoothness of the surface (*cf.* lowermost block in Fig. 12).

While the above test effectively highlights the impact of outliers on the reconstruction, we argue that it does not fully accurately reflect the statistical characteristics of noise emerging in real-world normal maps, in particular those predicted by learning-based methods. To provide an additional evaluation of the robustness of our method under noise in the input normals, we perturb the surface normals by rotating them around an axis that we randomly sample for each pixel, with an angle of rotation that we sample from a Gaussian distribution. Figure 13 shows the results of this ablation, where we vary the standard deviation of the Gaussian distribution between 1 and 10 degrees. Similarly to the experiment with outliers, providing the raw normal map as input to our method results in spike artifacts (second block from the top in Fig. 13). Noticeably, however, most of these artifacts can be corrected by average filtering of the pixels with invalid normals alone (third block from the top in Fig. 13), showing that physically impossible normals constitute the main factor behind these artifacts. As in the case with outliers, additionally filtering pixels where $|\mathbf{n}_a^\top \boldsymbol{\tau}_a|$ deviates largely from the mean value in the pixels’ neighborhood allows further reducing artifacts and removing spikes (lowermost block in Fig. 13).

I. Limitations

Robustness to noise. While effective mitigation strategies can be designed based on the value and the distribution of $\mathbf{n}_a^\top \boldsymbol{\tau}_a$, as shown in Appendix H our method is sensitive to noise in the input normals, producing spike artifacts for physically impossible normals. More robustly tackling these outliers is an interesting direction for future work. Possibilities include the addition of regularization terms to the optimization cost function or direct re-weighting of the formulation, with the previous analysis of [8] suggesting that re-balancing factors in the functionals might lead to increased numerical robustness. An alternative consists in ensuring that the input normals are physically meaningful (*i.e.*, $\mathbf{n}_a^\top \boldsymbol{\tau}_a < 0$) by design, as is the case for normals predicted by recent learning-based methods [4]: as demonstrated in Sec. 4.5, for these real-world inputs our method successfully produces reconstruction without spike artifacts.

Non-central camera models. Since it is based on ray direction vectors, our formulation does not allow handling camera models that are non-central, *i.e.*, that do not assume all camera rays to originate from a single point (such as axial cameras [27]). A particular case of non-central cameras

are orthographic cameras, which assume the center of projection to be at an infinite distance from the scene. As a consequence, in this model all ray direction vectors are parallel to each other and perpendicular to the image plane, *i.e.*, $\boldsymbol{\tau}_a = \boldsymbol{\tau}_b = \boldsymbol{\tau}_m = (0, 0, 1)^\top$ for all a, b, m . We note that in this case our formulation (2) reduces to $z_a = \varepsilon_{b \rightarrow a} + z_b$, which, while correct, does not depend on the surface normals and is thus not applicable to normal integration.

Run time and input size. Similarly to previous optimization-based approaches [6, 22, 25], our method is not compatible with real-time deployment, with optimization converging in a time frame in the order of several seconds (50 to 120 seconds for input normal maps of size 512×612). Additionally, like for previous approaches, our system matrix \mathbf{A} (*cf.* (1) in the main paper), albeit sparse, has both a number of rows and a number of columns that scale linearly with the number of valid pixels in the input normal map. This leads to larger processing time and memory usage for large input sizes, making it currently unsuitable for high-resolution maps and highly complex scenes. More optimized implementations could reduce runtime and memory usage. Investigating more substantial modifications that could move away completely from the drawbacks of optimization-based integration is an interesting direction, but falls outside the scope of this study.

Hyperparameters. Our method depends on a number of hyperparameters, namely the parameters q and ρ of our discontinuity activation term $\beta_{b \rightarrow a}^{(t)}$ (*cf.* (16) in the main paper), the parameter k controlling the sharpness of the bilateral weights $w_{b \rightarrow a}^{\text{BiNI}}$ (*cf.* (10) in the main paper), and the ray directions $\boldsymbol{\tau}_m$ that control our planarity assumption (*cf.* Sec. 3.1 in the main paper). While the default choices $k = 2$ and $\boldsymbol{\tau}_m = (\boldsymbol{\tau}_a + \boldsymbol{\tau}_b)/2$ consistently result in optimal results (*cf.* Tab. 3 and Appendix D), a certain degree of object specificity can be observed in $\beta_{b \rightarrow a}^{(t)}$, particularly in its parameter q (*cf.* Appendix E). Therefore, tuning the latter parameter might be desirable to achieve slight improvements in performance.